0830-L-02

XHAS 1.29/3-2:02-04

NASA Tech Briefs

National Aeronautics and
Space Administration

Electronic Components and Circuits

Electronic Systems

1-48

Physical Sciences

Materials

Computer Programs

Mechanics

Machinery

Fabrication Technology

Mathematics and Information Sciences

Life Sciences

2002-02174-MP C

INTRODUCTION

Tech Briefs are short announcements of innovations originating from research and development activities of the National Aeronautics and Space Administration. They emphasize information considered likely to be transferable across industrial, regional, or disciplinary lines and are issued to encourage commercial application.

Availability of NASA Tech Briefs and TSPs

Requests for individual Tech Briefs or for Technical Support Packages (TSPs) announced herein should be addressed to

National Technology Transfer Center
Telephone No. **(800) 678-6882** or via World Wide Web at **www2.nttc.edu/leads/**

Please reference the control numbers appearing at the end of each Tech Brief. Information on NASA's Commercial Technology Team, its documents, and services is also available at the same facility or on the World Wide Web at **www.nctn.hq.nasa.gov**.

Commercial Technology Offices and Patent Counsels are located at NASA field centers to provide technology-transfer access to industrial users. Inquiries can be made by contacting NASA field centers and program offices listed below.

NASA Field Centers and Program Offices

Ames Research Center
Carolina Blake
(650) 604-1754 or
cblake@mail.arc.nasa.gov

Dryden Flight Research Center
Jenny Baer-Riedhart
(661) 276-3689 or
jenny.baer-riedhart@dfrc.nasa.gov

Goddard Space Flight Center
George Alcorn
(301) 286-5810 or
galcorn@gsfc.nasa.gov

Jet Propulsion Laboratory
Marie McKenzie
(818) 354-2577 or
marie.mckenzie@jpl.nasa.gov

Johnson Space Center
Hank Davis
(281) 483-0474 or
henry.l.davis1@jsc.nasa.gov

John F. Kennedy Space Center
Jim Aliberti
(321) 867-6224 or
Jim.Aliberti-1@ksc.nasa.gov

Langley Research Center
Sam Morello
(757) 864-6005 or
s.a.morello@larc.nasa.gov

Glenn Research Center
Larry Viterna
(216) 433-3484 or
cto@grc.nasa.gov

George C. Marshall Space Flight Center
Vernotto C. McMillan
(256) 544-2615 or
vernotto.mcmillan@msfc.nasa.gov

John C. Stennis Space Center
Kirk Sharp
(228) 688-1929 or
technology@ssc.nasa.gov

NASA Program Offices
At NASA Headquarters there are seven major program offices that develop and oversee technology projects of potential interest to industry:

Carl Ray
Small Business Innovation Research Program (SBIR) & Small Business Technology Transfer Program (STTR)
(202) 358-4652 or
cray@mail.hq.nasa.gov

Dr. Robert Norwood
Office of Commercial Technology (Code RW)
(202) 358-2320 or
rnorwood@mail.hq.nasa.gov

John Mankins
Office of Space Flight (Code MP)
(202) 358-4659 or
jmankins@mail.hq.nasa.gov

Terry Hertz
Office of Aero-Space Technology (Code RS)
(202) 358-4636 or
thertz@mail.hq.nasa.gov

Glen Mucklow
Office of Space Sciences (Code SM)
(202) 358-2235 or
gmucklow@mail.hq.nasa.gov

Roger Crouch
Office of Microgravity Science Applications (Code U)
(202) 358-0689 or
rcrouch@hq.nasa.gov

Granville Paules
Office of Mission to Planet Earth (Code Y)
(202) 358-0706 or
gpaules@mtpe.hq.nasa.gov

BLANK PAGE

NASA TechBriefs

National Aeronautics and
Space Administration

April 2002
02-04

5 Electronic Components and Circuits

9 Electronic Systems

15 Physical Sciences

25 Materials

29 Computer Programs

33 Mechanics

39 Machinery

45 Mathematics and Information Sciences

51 Life Sciences

This document was prepared under the sponsorship of the National Aeronautics and Space Administration. Neither the United States Government nor any person acting on behalf of the United States Government assumes any liability resulting from the use of the information contained in this document, or warrants that such use will be free from privately owned rights.

BLANK PAGE

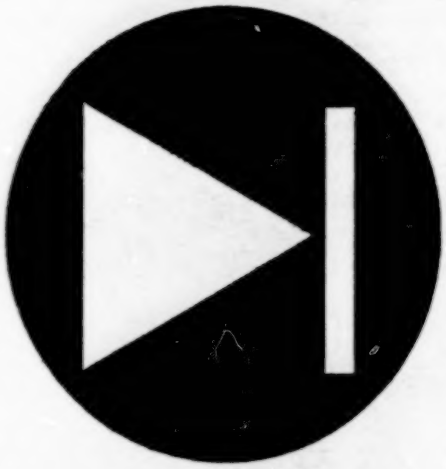

Electronic Components and Circuits

Hardware, Techniques, and Processes

7 Concept for Utilizing Full Areas of STJ Photodetector Arrays

8 Enabling Higher-Voltage Operation of SOI CMOS Transistors

BLANK PAGE

Concept for Utilizing Full Areas of STJ Photodetector Arrays

Also, cross-talk among pixels and the number of contacts would be reduced.

NASA's Jet Propulsion Laboratory, Pasadena, California

A method of designing improved monolithic planar arrays of superconducting tunnel junctions (STJs) for use as photodetectors has been conceived. These arrays would be suitable for detecting images at low light levels. They are for operation in the individual-photon-counting regime; they are used not only to detect the arrival of individual photons but also to measure the individual photon energies. As such, the STJ arrays would be compact sensors that would perform the functions now performed by bulkier equipment in the form of photomultipliers and spectrometers. Eventually, it should be possible to use STJ arrays for such demanding applications as simultaneous imaging and spectroscopy of faint astronomical objects.

Usually, an STJ photodetector contains three superconductors with different superconducting energy gaps. Photons in the energy range of interest are absorbed in the superconductor with the intermediate energy gap; this superconductor and the one with the lowest energy gap are separated by a layer of electrical insulation thin enough that photoexcited quasi-particles can tunnel (in the quantum-mechanical sense) through it. Together, the intermediate- and lowest-energy-gap superconductors and the insulating layer between them constitute the detector junction. The superconductor with the highest energy gap is used for wiring to the other two superconductors. In a typical previously developed STJ array, separate electrical connections are made to each photodetector (see Figure 1).

Even an abbreviated explanation of the present method and the ways in which it differs from older STJ-array-design methods would greatly exceed the scope of this article because it would unavoidably include complex and interdependent details of the physics and the fabrication of STJ devices in general. For the purpose of this article, it must suffice to summarize the major distinguishing features:

- In the previously developed STJ photodetector arrays, pixels are separated by small gaps, through which photons can pass undetected. These gaps can amount to significant fractions of total detector areas; in other words, overall quantum efficiencies are lower than they would be if full detector areas were utilized. In STJ arrays according to the present method (see Figure 2), the gaps between pixels would be either

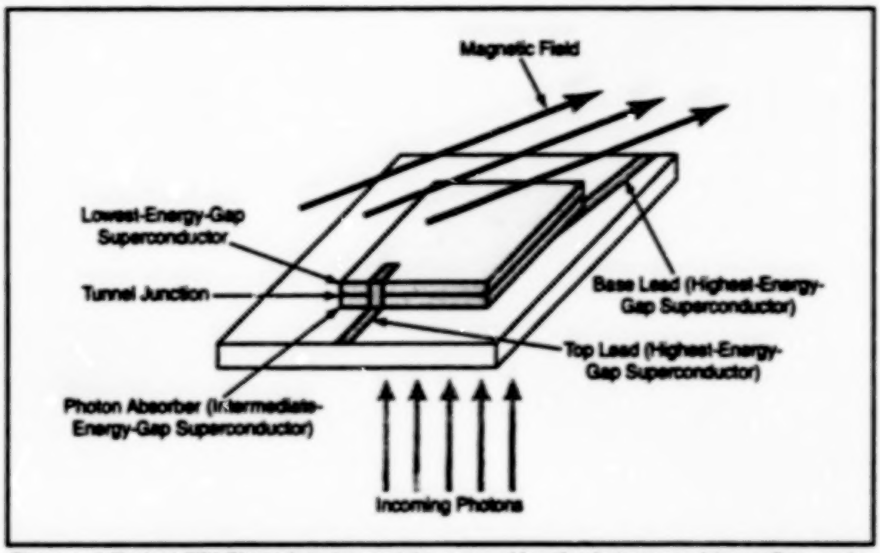

Figure 1. A Typical STJ Photodetector contains a tunnel junction between an intermediate- and a low-energy-gap superconductor. The electrical connections to the device are made via the base and top leads, which are made of a higher-energy-gap superconductor.

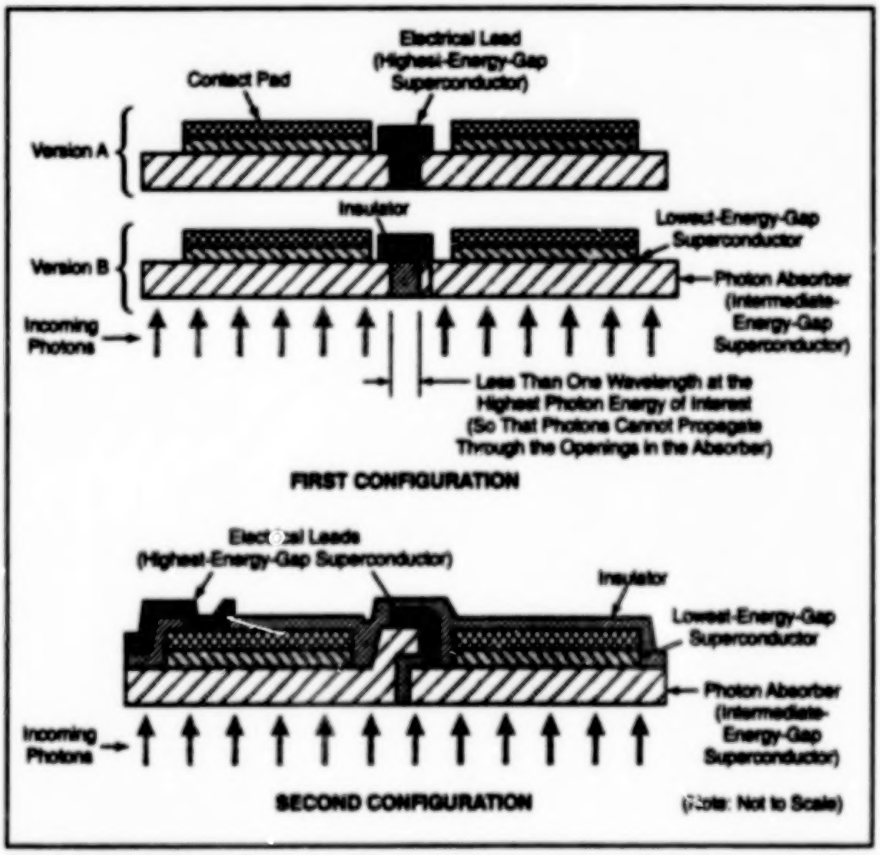

Figure 2. Two Adjacent Pixels of an STJ photodetector array according to the present method could be fabricated in either of two basic alternative configurations. In both configurations, the structure would behave like a solid ground plane for incident radiation at frequencies from dc up through hundreds of gigahertz, yet would present all (in the second configuration) or nearly all (in the first configuration) of its area for absorption of photons in the energy range of interest.

negligibly small or entirely absent; in other words, full detector areas would be utilized, thereby maximizing quantum efficiencies.

- In a typical previously developed STJ array of m rows and n columns, the number of electrical contacts necessary for individual biasing and readout of all pixels is 2mn because two contacts are needed for each pixel. In an STJ according to the present method, the number of contacts needed would be mn + 1 (slightly more than half the number previously needed) because the photon-absorbing (intermediate-energy-gap) superconductors of all the pixels would be electrically tied together by the largest-energy-gap superconductor.
- Even though the full detector area would be utilized in the present method, the pixels would be electrically isolated from each other with respect to diffusion of photoexcited quasi-particles between superconductors, so that cross-talk among pixels would be suppressed.
- Unlike at least one prior method, the present method does not call for small superconducting bridges among neighboring pixels. This is an advantage in that such bridges could, potentially, constitute undesired superconductive magnetic-flux-trapping loops.

This work was done by Michael Burns of Caltech for **NASA's Jet Propulsion Laboratory**. *Further information is contained in a TSP [see page 1].*
NPO-20768

Enabling Higher-Voltage Operation of SOI CMOS Transistors

An integrated-circuit substrate would be biased against turn-on of parasitic transistors.

NASA's Jet Propulsion Laboratory, Pasadena, California

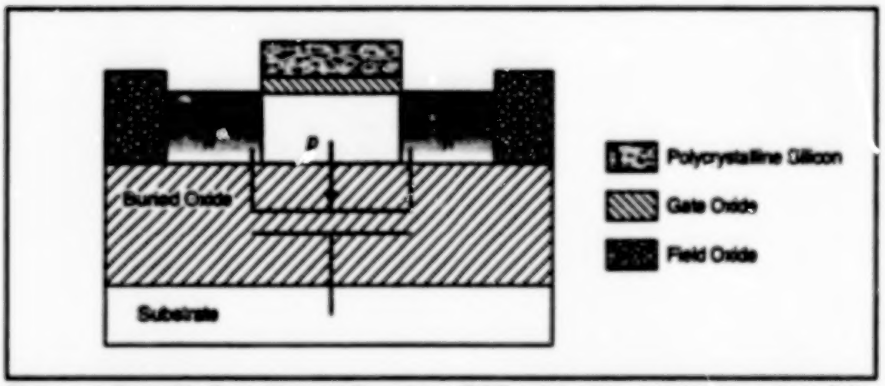

Figure 1. A Parasitic Back-Channel Transistor (BCT) exists under a typical low-voltage field-effect transistor (FET). If a high voltage is impressed on the source or drain of this FET, an inversion layer can form just above the buried oxide, allowing current to flow.

A "smart" back-gate driver circuit has been proposed to enable the operation, at voltages higher than were previously possible, of a silicon-on-insulator (SOI) complementary metal oxide/semiconductor (CMOS) integrated circuit that contains both low- and high-voltage transistors energized by corresponding low- and high-voltage power supplies. As used here, "low voltage" signifies potentials ≤3.3 V, while "high voltage" signifies potentials ≥40 V. The purpose of the back-gate driver circuit is to raise the threshold (turn-on) voltages of parasitic back-channel transistors (BCTs) that unavoidably exist in such an integrated circuit (see Figure 1). Turn-on of the parasitic transistors is unacceptable because it causes short circuits that render the integrated circuit inoperative.

In a mixed-voltage (high-voltage/low-voltage) SOI CMOS integrated circuit, the turn-on threshold voltages of parasitic BCTs are usually less than the voltage that the high-voltage transistors can withstand; heretofore, this fact has made it necessary to limit voltage ratings accordingly. The problem is complicated by the fact that ionizing radiation causes the accumulation of positive charges in the buried oxide layer of the integrated circuit, and these charges lower the threshold voltages of the parasitic BCT.

The proposed back-gate driver circuit would apply, to the integrated-circuit substrate, a bias voltage that would ensure that the parasitic BCTs remain in the "off" state at voltages beyond those that would otherwise cause the parasitic transistors to turn on. The proposed back-gate driver circuit is characterized as "smart" because it would sense the effect of ionizing radiation on the threshold voltages and would respond by adjusting the bias voltage that it applies so as to maximize the margin of turn-off of the parasitic transistors.

Figure 2 is a simplified schematic diagram of the proposed circuit. A current of 1 μA would be forced through one n-type back-channel transistor (BCT). The source of this BCT would be biased to –5 V to ensure that its gate-to-source voltage (V_{gs}) was 5 V greater than that of any other n-type BCT on the integrated-circuit chip. Feedback would force this V_{gs} to a level that would cause a current of 1 μA to flow in this one BCT. This V_{gs} would slightly

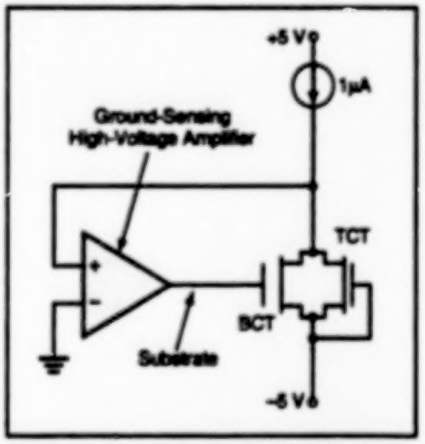

Figure 2. The "Smart" Back-Gate Driver Circuit would sense the turn-on voltage of one parasitic BCT and respond by biasing the substrate at a voltage that would keep all the other parasitic BCTs turned off. (Note: TCT = top-channel transistor.)

exceed the turn-on voltage of this BCT, forcing the substrate voltage to be approximately 5 V less than the turn-on voltages of all other n-channel BCTs on the chip. Exposure of the integrated circuit to aging would cause the turn-on voltages of the both the p- and n-type BCTs to shift in the same direction by about the same amount. Thus, by shifting the substrate-bias voltage in response to the sensed turn-on of one n-type BCT, the proposed circuit would maintain voltage margins against turn-on of both the remaining n-type BCTs and all the p-type BCTs.

This work was done by Mohammad Mojarradi of Caltech, Benjamin Blalock of Mississippi State University, and Harry Li of the University of Idaho for **NASA's Jet Propulsion Laboratory**. *For further information, access the Technical Support Package (TSP)* ***free on-line at www.nasatech.com*** *under the category.*
NPO-20910

Electronic Systems

Hardware, Techniques, and Processes

11 Fiber-Optic Rotary Joint for Passing High-Definition Video
11 Adaptive Multiplexing for Free-Space Optical Communication
12 Estimating Antenna-Pointing Errors From Beam Squints

Books and Reports

13 Development of Cognitive Sensors

BLANK PAGE

Fiber-Optic Rotary Joint for Passing High-Definition Video

Fiber-optic transmission overcomes the bandwidth limitation of slip rings.

Dryden Flight Research Center, Edwards, California

Camera Integrated With Tracking Pedestal

Fiber-Optic Rotary Joint

The Integration of the Camera With the Tracking Pedestal was made possible by modification of the pedestal and development of the FORJ.

A video camera has been integrated with a tracking pedestal (see figure) for tracking of aircraft and spacecraft. The camera is of a high-definition (1,280 × 720 pixels), progressive-scan, 60-frame-per-second digital type that conforms to NASA Standard 2818 (Digital Television Standards for NASA, a copy of which can be obtained via the Internet at *http://www.hq.nasa.gov/office/oio/standards/2818.pdf*). The camera is mated to a 13.5-to-1,755-mm zoom lens, making it possible to track vehicles at distances up to 100 miles (~160 km).

The digital video signal, at a data rate of 1.5 Gb/s, is transmitted from the camera via an optical fiber. The signal passes through a fiber-optic rotary joint (FORJ) through the horizontal axis of rotation of the pedestal. The FORJ contains two fiber-optic conductors, each capable of a data rate of 3 Gb/s, that are used to pass high-definition video and camera-control signals. All other power and control signals pass through standard copper slip rings in the pedestal.

The FORJ and the pedestal are commercial products. The pedestal was modified to accept the FORJ. The modification included the fabrication of a yoke assembly to enable rotation of the upper half of the FORJ with the rotation of the upper half of the pedestal. The FORJ was originally produced for use in submersible remotely operated vehicles with rotating manipulator arms. The high-bandwidth digital video signal cannot pass through conventional copper slip rings of the unmodified tracking pedestal. The modification of the tracking pedestal to work with the FORJ makes it possible to use high-definition video for tracking experimental aircraft and spacecraft.

This work was done by Tony Trent of **Dryden Flight Research Center**.

DRC-01-28

Adaptive Multiplexing for Free-Space Optical Communication

Wavelength- and code-division multiplexing would be utilized for security and improved performance.

NASA's Jet Propulsion Laboratory, Pasadena, California

"Laser-based adaptive wavelength division multiplexing and code division multiplexing" (LAWDM-CDM) is the name of a method that has been proposed to increase security, signal-to-noise ratios (SNRs), redundancy, and adaptability in free-space optical communications. The need for this or a similar method arises as follows:

- In free-space optical communications, various phenomena can affect the propagation and reception of laser beams; these phenomena include jitter of

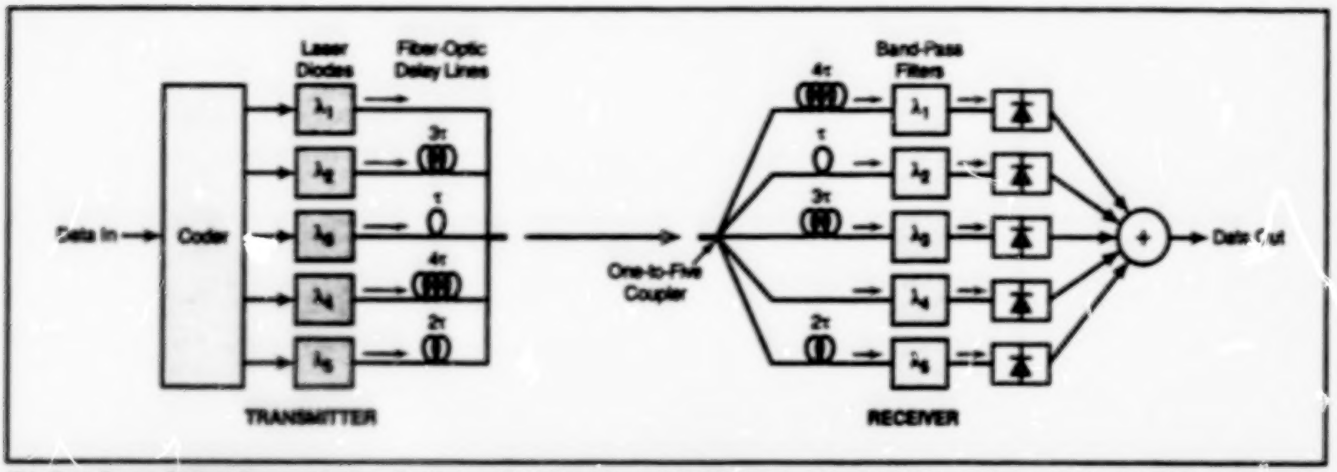

This Free-Space Optical Communication System would implement a combination of wavelength-division and time-spread code-division multiplexing.

transmitter and receiver platforms and atmospheric attenuation and distortion of laser beams. In a conventional free-space optical communication system, data are transmitted at a constant rate that is not changed to adapt to changing conditions; consequently, for example, a sudden change in weather can disable the free-space optical link, causing loss of data.

- Free-space optical communications are not entirely secure because laser beams can propagate beyond intended receivers and therefore can be intercepted by unintended parties.

In addition to wavelength-division and code-division multiplexing, LAWDM-CDM would involve the use of multiple transmitting apertures, adaptive control of the data-transmission rate and the transmitter power, and other advanced techniques as described below.

- Eavesdropping would be reduced by using adaptive optics to reduce atmosphere-induced beam spreading and by tailoring the transmitter power to be low enough to minimize propagation beyond the intended receiver yet high enough to reach the intended receiver with an acceptably high SNR. One could choose wavelengths with limited atmospheric transmission to reduce the range of the optical signal.
- Wavelength hopping and code-division multiplexing would make it difficult for an unintended recipient to decode a signal.
- Under adverse atmospheric conditions, the bit rate would be reduced to keep the bit-error rate below a specified maximum acceptable level.
- At the transmitter, laser light back-scattered by the atmosphere would be detected in a lidarlike subsystem, the output of which would be utilized in an algorithm that would select the optimum bit rate and power level.
- Multiple apertures at a transmitter would help to reduce the effect of the scintillation.
- Time-spread code-division multiplexing would enhance reception.

The figure illustrates an example of a simple system that would utilize a combination of wavelength-division multiplexing and time-spread code-division multiplexing to increase security. In the transmitter, a code sequence comprising five parallel bits during each bit period would control the simultaneous generation (for "1") or non-generation (for "0") of pulses by five laser diodes, each operating at a different one of five wavelengths (λ_1 through λ_5). Before being launched for propagation to the receiver, the signal in the ith wavelength channel would be delayed by an amount τ_i, which would be a unique integer multiple of the bit period, τ. The longest delay would be 4τ for λ_4.

In order to be able to decode the signal properly, the receiver would have to be equipped with delay lines complementary to those in the transmitter: In the receiver, the incoming signal would be demultiplexed into the five wavelength channels and the signal in the ith channel would be delayed by $4\tau-\tau_i$, so that the total of transmitter and receiver delays in each channel would be 4τ and, hence, the five signals would come out of the receiver simultaneously, just as the original five bits went into the transmitter simultaneously.

Provided that the differences among the five wavelengths were sufficiently large and the transmitter power were properly adjusted, this system would offer a security advantage in that it would be difficult for an unintended recipient to detect its operation. Moreover, eavesdropping on any single wavelength would not enable one to decode the message.

This work was done by Sir B. Reid and Keith Wilson of Caltech for **NASA's Jet Propulsion Laboratory.** *Further information is contained in a TSP [see page 1].*
NPO-20890

Estimating Antenna-Pointing Errors From Beam Squints

RCP and LCP beams are received at different levels when aim is not perfect.

NASA's Jet Propulsion Laboratory, Pasadena, California

A method of estimating the pointing error of an offset-conic-section reflector antenna equipped to receive in both right circular polarization (RCP) and left circular polarization (LCP) exploits a phenomenon that, heretofore, has been regarded as a minor nuisance. The phenomenon in question is a misalignment between RCP and LCP beams and manifests itself as opposing squints of the beams. The method enables the generation of pointing-error estimates at high rates for use as feedback in high-bandwidth antenna tracking-control systems, without need for the complex radio-frequency circuitry of monopulse or traditional sequential-lobing antenna tracking-control systems. The method was conceived especially to be

used at terrestrial stations to track LCP and RCP signals transmitted by satellites.

When an antenna is mispointed in one direction, the RCP signal normalized by its peak value is stronger than the corresponding normalized value of the LCP signal. When the antenna is mispointed in the opposite direction, the normalized LCP signal is the stronger one. Zero pointing error in this context is defined as the antenna-aiming direction for which the normalized RCP and LCP signal levels are equal. The difference between normalized signal levels can be characterized as an S-curve function of the pointing error; this curve is given by

$$S(\phi) = 2\{[R(\phi)/R_p] + [L(\phi)/L_p]\}/\{[R(\phi)/R_p] - [L(\phi)/L_p]\},$$

where ϕ is the angular pointing error; $R(\phi)$ and $L(\phi)$ denote the levels of the RCP and LCP signals, respectively, at ϕ; and R_p and L_p denote the peak levels of these signals. The figure presents an example of the normalized signal levels and of the S-curve function for small pointing-error angles. The S-curve function can be inverted so that the pointing error can be estimated from the normalized signal levels.

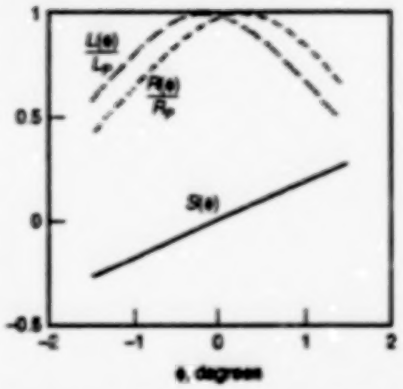

These Curves Were Calculated for Gaussian RCP and LCP beams 3° wide, with 0.3° squint between beams.

In the present method, one obtains the normalized signal levels from measurements of levels and differences between levels of satellite signals received through the antenna while switching rapidly (electronically) between the reception in RCP and LCP. "Satellite dish" antennas equipped with circuitry to receive both RCP and LCP and capable of rapid switching between RCP and LCP are commercially available. This method of reception amounts, in effect, to a method of electronic sequential lobing. The faster the electronic switching between RCP and LCP, the greater the bandwidth of the pointing-error signal.

This work was done by Arthur Densmore of Caltech for **NASA's Jet Propulsion Laboratory**. *Further information is contained in a TSP [see page 1].*

This invention is owned by NASA, and a patent application has been filed. Inquiries concerning nonexclusive or exclusive license for its commercial development should be addressed to the Patent Counsel, NASA Management Office-JPL [see page 1]. Refer to NPO-19938.

Books and Reports

Development of Cognitive Sensors

A technical report enunciates the concept of a hierarchy of sensor classes (meaning transducers, associated circuitry, and embedded software) that have different levels of intelligence, and discusses issues pertaining to the development of sensors of the highest level of intelligence, called cognitive. The other levels, in order of decreasing intelligence, belong to the class of intelligent or smart sensors. A design process and an intelligence hierarchy which enables construction of intelligence-based sensors has been developed based on five main qualities:

1. self-knowledge — the sensor must identify its purpose and understand its operational functions;
2. communication — the sensor must be capable of transmitting/receiving information (versus raw data) to/from other devices;
3. perception — the sensor must have the ability to recognize, interpret, and understand sensory stimuli;
4. reasoning — the sensor must be capable of making decisions based on perception of sensory stimuli; and
5. cognition — the sensor's intellectual process must subscribe to the process of knowing, which includes aspects such as awareness, perception, reasoning, and judgement.

The report discusses hardware and software of a cognitive sensor in general and, more specifically, of sensors for use in planetary exploration. A generic process for designing the hardware and software of a cognitive sensor is described. Specific instances are described for the examples of (1) an optoelectronic sensor that recognizes a moving object and includes a camera that tracks the object and (2) a similar optoelectronic sensor that recognizes rocky terrain, determines the safest path across the terrain on the basis of the sizes and distribution of rocks, and aims the camera along this path.

This work was done by Ayanna Howard and Edward Tunstel of Caltech for **NASA's Jet Propulsion Laboratory**. *To obtain a copy of the paper, "Cognitive Sensor Technology," see TSP's [page 1].*

NPO-30283

BLANK PAGE

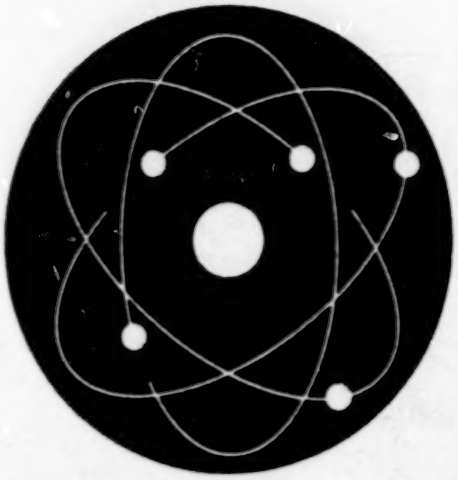

Physical Sciences

Hardware, Techniques, and Processes

17 Planetary Rover Absolute Heading Detection Using a Sun Sensor
18 Electrometer for Triboelectric Evaluation of Materials
19 Refractive Secondary Concentrators for Solar Thermal Systems
20 Model of a Fluidized Bed Containing a Mixture of Particles
21 Making Three-Dimensional Holograms Visible From All Sides
22 Multiple-Path-Length Optical Absorbance Cell
23 Cold Flow Calorimeter
23 Infrared CO_2 Sensor With Built-In Calibration Chambers
23 Solid-State Potentiometric CO Sensor

Books and Reports

24 Characteristics of Supercritical Transitional Mixing Layers

BLANK PAGE

Planetary Rover Absolute Heading Detection Using a Sun Sensor

Headings are accurate to within a few degrees.

NASA 's Jet Propulsion Laboratory, Pasadena, California

A relatively inexpensive Sun sensor for determining the absolute heading of planetary rovers to within ± 3° using a monochrome charge-coupled device (CCD) camera is presented. The Sun sensor was developed for the Field Integrated, Design and Operations (FIDO) rover. This rover is an advance technology rover that is a terrestrial prototype of the rovers that NASA/JPL plans to send to Mars in 2003. The goal of the FIDO team was to develop a Sun sensor that fills the current cost/performance gap, uses the power of sub-pixel interpolation, makes use of current hardware on the rover, and demands very little computational overhead. In addition, a great deal of emphasis was placed on robustness to calibration errors and the flexibility to make a transition to a new rover with very little modification.

The resulting Sun sensor, which is shown in Figure 1, consists of a CCD monochrome camera, two neutral-density filters, a wide-angle lens, and housing. The neutral-density filters reduce incident light to capture only the Sun's disk. The Sun sensor camera is modeled as a fish-eye camera/lens system with 21 parameters; the parameters are computed in the calibration procedure that can be performed easily and even "on the fly." The Sun sensor captures images of the Sun using an onboard frame grabber mounted on the rover-computing stack. The centroid of the Sun in the image is the main feature needed for determination of the rover heading. Centroid extraction follows a three-step process: thresholding, artifact removal, and center of mass/circularity determination. From the Sun centroid a 3-D unit ray vector is computed from the sensor frame to the Sun using the camera model. The 3-D vector is then transformed into a gravity-down rover reference frame by use of the roll- and pitch-angle outputs of an inertial sensor that is part of the onboard rover navigation system. The azimuth and elevation of the Sun with respect to the rover reference frame are then determined. By use of solar ephemeris data and the equation of time from the Astronomical Almanac, the azimuth and elevation of the Sun are determined for the applicable longitude, latitude, and universal time (UT). The UT is obtained from the rover computer clock and corrected to the nearest second. Finally, the heading with respect to true north is computed by use of the known relationship between (1) the azimuth and elevation of the Sun as computed from

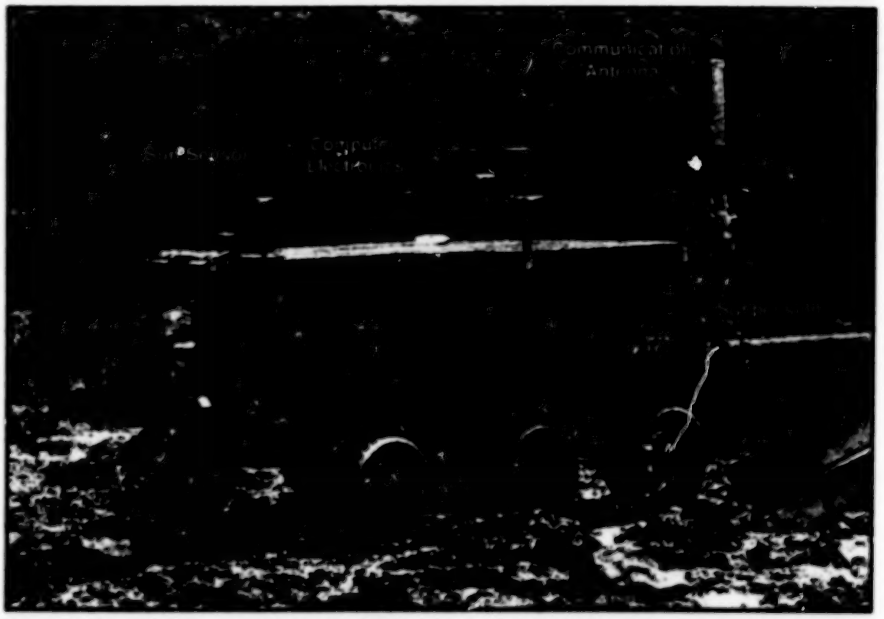

Figure 1. **Sun Sensor** mounted on the FIDO rover is used for determining the absolute heading within ±3°.

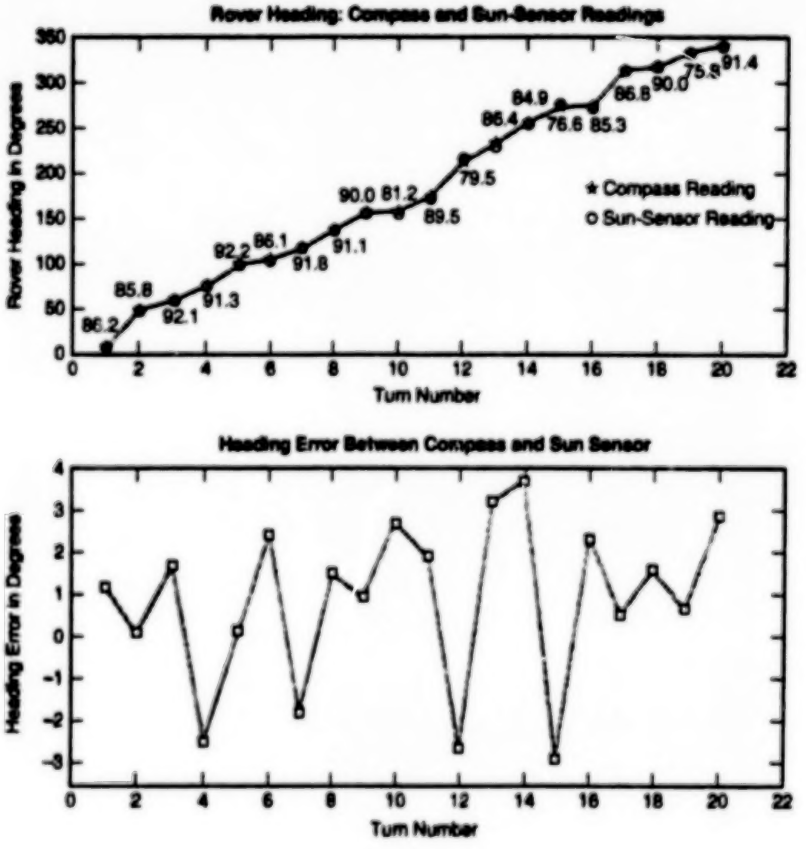

Figure 2. **Plots of Rover Heading From Compass and Sun Sensor** are illustrated. Unlike in an odometry-based heading estimation, in a Sun-sensor-based heading estimation the relative rover heading error is a constant.

the ephemeris data and (2) the azimuth and elevation of the Sun as determined from the Sun-sensor data.

In a test of the Sun sensor mounted on the FIDO rover, the rover was placed on a flat surface and turned in place at angular increments of about 20°. Figure 2 depicts the headings as measured by the Sun sensor and by a magnetic compass, as well as the differences between them. The Sun sensor confidence for each reading is also indicated on the plot. The accuracy of the magnetic compass used is ± 2°. The differences between the readings can be attributed to several factors, including mechanical alignment errors of the Sun sensor, rover attitude errors, and atmospheric conditions (cloud cover).

Results of a recent FIDO field trial at Black Rock Summit in Central Nevada, in May of 2000 and several Operations Readiness Tests (ORTs) at the JPL Mars Yard using the Sun sensor have demonstrated three- to four-fold improvement in the heading estimation of the rover compared to incremental odometry. These test results helped shape the mission specifications outlined by NASA for the 2003 mission to Mars.

This work was done by Ashitey Trebi-Ollennu, Terry Huntsberger, Brett Kennedy, and Eric Baumgartner of Caltech for **NASA's Jet Propulsion Laboratory.** *For a full report on the Sun sensor visit http://fido.jpl.nasa.gov/publications.*

NPO-21182

Electrometer for Triboelectric Evaluation of Materials

Some materials should be distinguishable by their triboelectric responses.

NASA's Jet Propulsion Laboratory, Pasadena, California

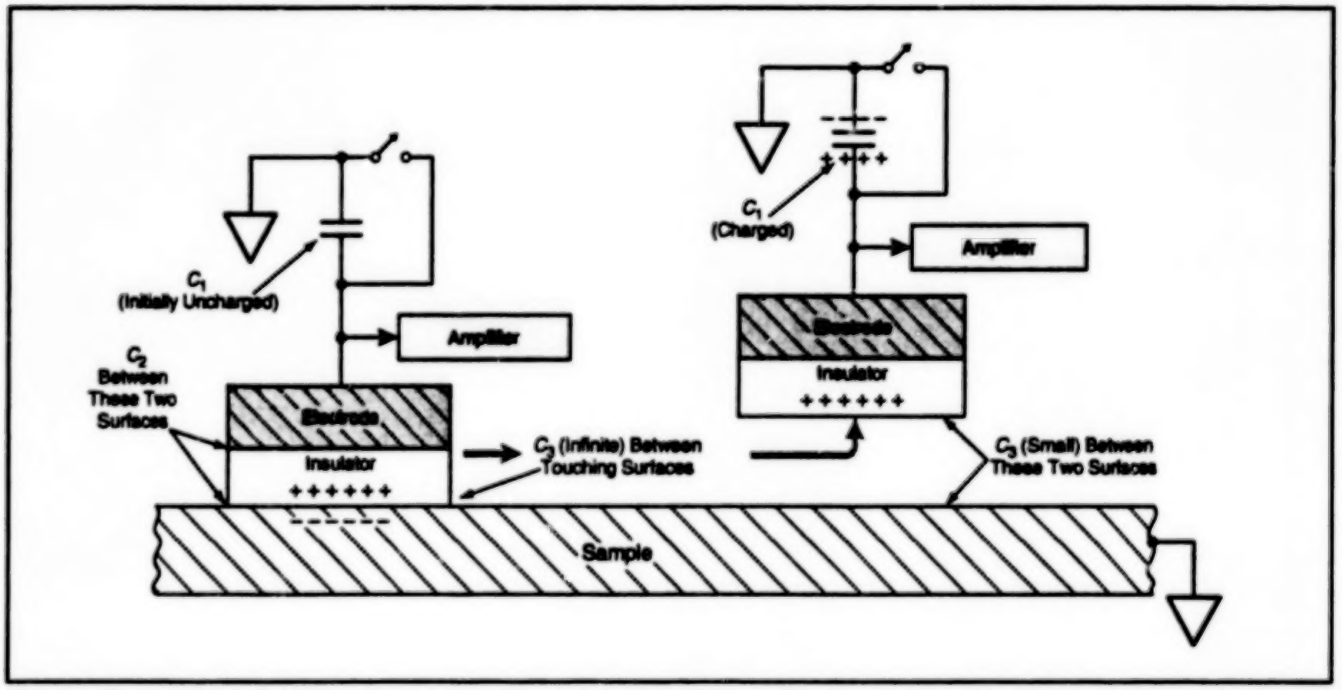

Figure 1. The Insulator Is Rubbed along the surface of the sample, then withdrawn. The rise and decay of the triboelectric charge induced by the rubbing is indicated by the time-varying output voltage of the amplifier.

An electrometer developed for measuring the triboelectric responses of soils on Mars is also potentially useful on Earth for identifying some materials via their triboelectric responses. In operation, an array of triboelectric sensors is rubbed against the material of interest for a predetermined distance, then withdrawn from the material of interest at a predetermined speed. During this operation, the electrometer circuitry measures the time-varying sensor output voltages, which are proportional to the electric charges induced on the sensors by the rubbing. The resulting voltage-vs.-time data constitute the desired triboelectric-response data. If materials that one seeks to identify or to distinguish from each other exhibit unique, known triboelectric responses that have been catalogued, then a sample of unknown material can be identified by seeking a match between its triboelectric response and one of the catalogued responses.

Figure 1 is a simplified schematic depiction of one of the triboelectric sensors connected to a charge-sensing circuit (charge-to-voltage converter). This converter is a conventional electrometer circuit that includes a capacitor (C_1) and an operational amplifier in a follower configuration. The triboelectric sensor is an electrode covered with a layer of insulating material. The outer surface of the insulating material is what is rubbed against the material of interest.

The capacitance between the outer surface of the insulator and the electrode is C_2. The voltage associated with the triboelectric charge that accumulates on the rubbed insulator surface is coupled, via this capacitance, to the C_1/amplifier node. Initially during rubbing, the switch shown in Figure 1 is kept closed to prevent C_1 from charging, thereby constraining the electrometer input and output voltages to be zero. At a designated point during rubbing, the switch is opened, allowing C_1 to charge and the electrometer output voltage to depart from zero.

The triboelectric response — that is, the electrometer output voltage as a function of time — depends on several factors, including the following:

- The triboelectrically induced charge (Q_t) present at the instant of liftoff following rubbing;
- C_1, C_2, and amplifier-circuit resistances;

- The speed of withdrawal;
- The time-varying capacitance C_3 between the rubbed insulator and sample surfaces; and
- The electrical resistivities of the insulator and sample materials.

Figure 2 shows triboelectric responses from an experiment in which five sensors made with five different insulating materials were rubbed against wool felt.

Electrometers based on this concept might be useful in industrial settings for inspecting and identifying incoming materials; for example, to identify fabrics coming into a clothing factory. Another potential use could be distinguishing between contaminated and uncontaminated soils. Another application might be evaluating moisture contents of soils; this should be possible because the rate of decay of triboelectric charge depends on humidity.

This work was done by Martin Buehler and Raymond Gompf of Caltech for **NASA's Jet Propulsion Laboratory.** *Further information is contained in a TSP [see page 1].*

In accordance with Public Law 96-517, the contractor has elected to retain title to this invention. Inquiries concerning rights for its commercial use should be addressed to

Intellectual Property group
JPL
Mail Stop 202-233
4800 Oak Grove Drive
Pasadena, CA 91109
(818) 354-2240

Refer to NPO-20684, volume and number of this NASA Tech Briefs *issue, and the page number.*

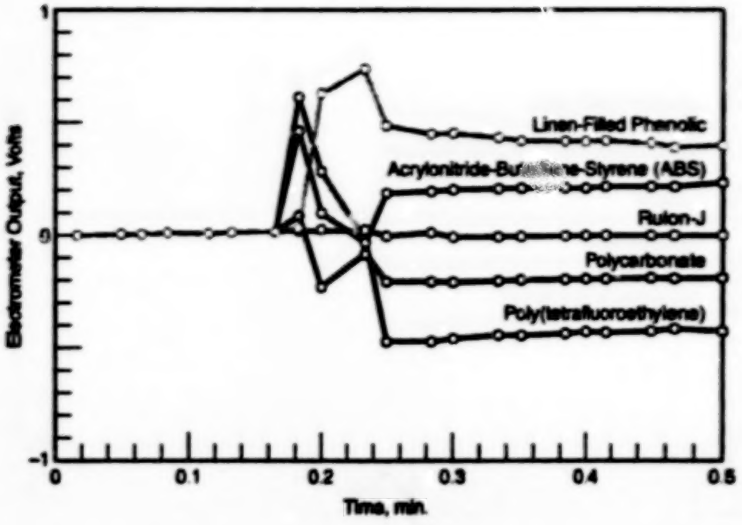

Figure 2. These Five Triboelectric Responses were obtained from rubbing five triboelectric sensors against wool felt. The insulators on the sensors were made from the noted materials.

Refractive Secondary Concentrators for Solar Thermal Systems

Concentration ratios as high as 10^4 and operating temperatures >2,000 K are anticipated.

John H. Glenn Research Center, Cleveland, Ohio

High-throughput, non-imaging, secondary concentrating optics that utilize refraction and total internal reflection are undergoing development for use in conjunction with advanced primary solar concentrators to provide solar thermal energy for space applications. This development is prompted by (1) a need to concentrate sunlight by factors of as much as 10^4 to satisfy design and operating requirements for some advanced solar thermal systems and (2) the impracticality of fabricating primary concentrators with sufficient precision to afford such high concentration ratios by themselves. Figure 1 illustrates the operation of a refractive secondary concentrator.

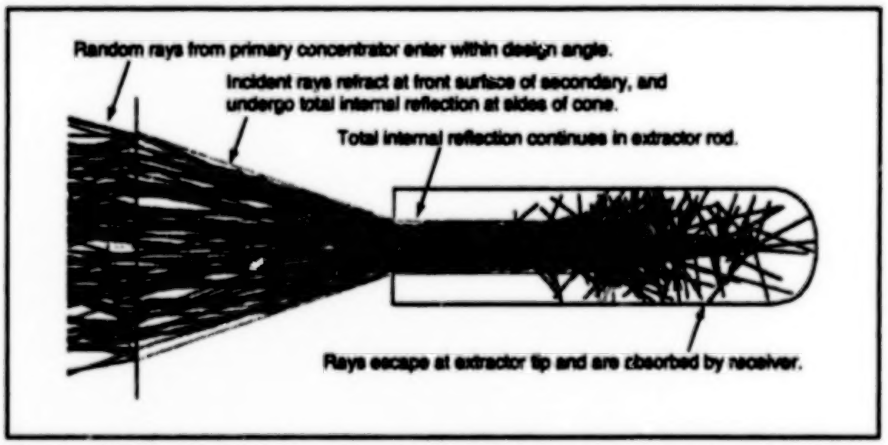
Random rays from primary concentrator enter within design angle.
Incident rays refract at front surface of secondary, and undergo total internal reflection at sides of cone.
Total internal reflection continues in extractor rod.
Rays escape at extractor tip and are absorbed by receiver.

Figure 1. A Refractive Secondary Concentrator efficiently concentrates solar energy from a primary concentrator then allows the energy to escape onto a receiver cavity.

The innovative refractive secondary concentrator offers significant advantages over all other types of secondary concentrators. The refractive secondary offers the highest throughput efficiency, provides for flux tailoring, requires no active cooling, relaxes the pointing and tracking requirements of the primary concentrator, and enables very high system concentration ratios. This technology has broad applicability to any system that requires the conversion of solar energy to heat, including electric power generation, thermal propulsion and high temperature furnaces. NASA Glenn initiated the development of the refractive secondary concentrator in support of Shooting Star, a solar thermal propulsion flight experiment, and continued the development in support of Space Solar Power.

A prototype sapphire refractive secondary concentrator (see Figure 2), has completed solar vacuum performance testing using a liquid-cooled calorimeter in NASA Glenn's Tank 6 facility. The effort involved the design and fabrication of a sapphire refractive secondary concentrator, design and fabrication of a calorimeter and its support systems, calibration of

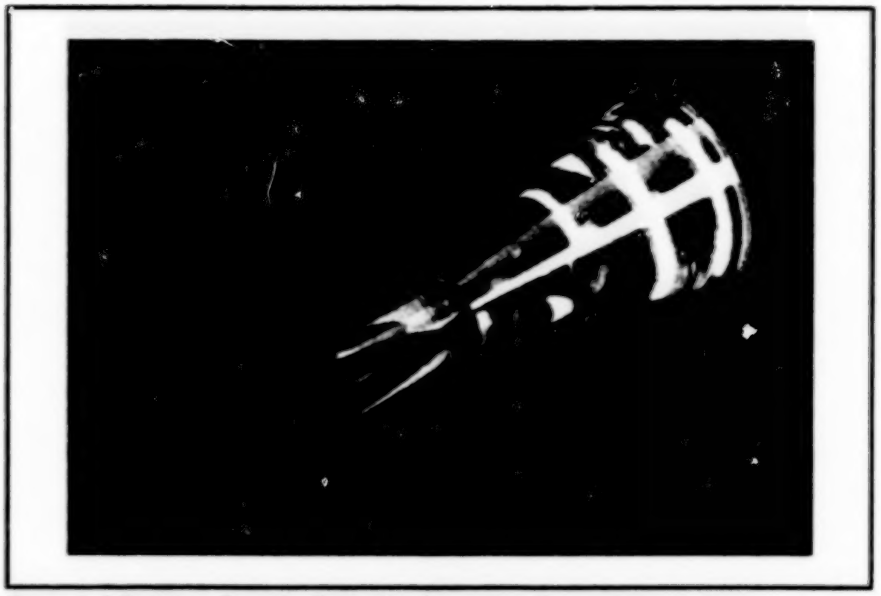

Figure 2. A Prototype Sapphire Refractive Secondary Concentrator is shown.

the calorimeter, on-sun vacuum testing of the refractive secondary, and comparing the test results with modeling predictions.

The prototype refractive secondary concentrator, measuring 3.5 in. (8.9 cm) in diameter and 11.2 in. (28.5 cm) long, was designed for the Tank 6 facility and the existing primary concentrator/solar simulator system. Ray trace optics software was used to model the secondary concentrator resulting in predicted efficiency without an antireflective coating of 90 percent. The solar vacuum test results indicate an average throughput efficiency of 87 percent, which agrees well with the modeling predictions. It is anticipated that reduction of a known reflection loss off of the inlet surface by applying an antireflective coating to that surface would result in a secondary concentrator throughput efficiency of approximately 93 percent. Potential future activities to further develop the technology include high temperature, high power throughput tests, antireflective coating tests, and additional material characterization and interaction tests.

This work was done by Wayne A. Wong and Steven M. Geng of **Glenn Research Center** *and Robert P. Macosko and Charles H. Castle of the Analex Corporation. Further information is contained in a TSP [see page 1].*

Inquiries concerning rights for the commercial use of this invention should be addressed to NASA Glenn Research Center, Commercial Technology Office, Attn: Steve Fedor, Mail Stop 4–8, 21000 Brookpark Road, Cleveland, Ohio 44135. Refer to LEW-17149.

Model of a Fluidized Bed Containing a Mixture of Particles

Predictions thus far are in reasonable agreement with experimental data.

NASA's Jet Propulsion Laboratory, Pasadena, California

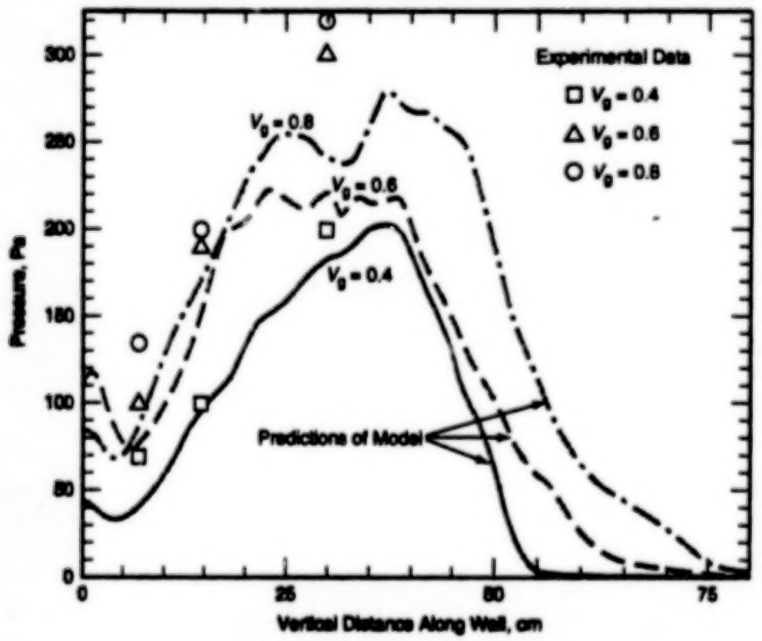

The Time-Averaged Solids Pressure as a function of height along the wall of a bed of glass beads fluidized with air was computed by the model and measured at superficial gas speeds of 0.4, 0.6, and 0.8 m/s. (The beads had a diameter of 0.5 mm and a density of 2.5 g/cm³, the channel had a square cross section 12.7 × 12.7 cm, and the bed was initially filled with beads to a depth of 43 cm.)

A mathematical model has been developed for use in analyzing the dynamics of an isothermal, non-chemically-reacting mixture of particles in a bubbling fluidized bed. Although the model has generic validity, it is intended, more specifically, to be applied to a fluidized bed that contains a mixture of sand and biomass particles, fluidized by steam. The model includes components in common with the models described in "Model of Pyrolysis of Biomass in a Fluidized-Bed Reactor (NPO-20708), *NASA Tech Briefs*, Vol. 25, No. 6 (June 2001), page 59 and Multiphase-Flow Model of Fluidized-Bed Pyrolysis of Biomass (NPO-20789), *NASA Tech Briefs*, Vol. 26, No. 2 (February 2002), page 56.

The derivation of the model follows a multifluid approach according to which macroscopic transport equations are derived by taking suitable ensemble averages of the equations for the local dynamics of the gas and particle phases. A standard phasic ensemble average is selected for the gas phase. For the particles, transport equations for each particle species (e.g., a set of equations for sand and another for biomass) are derived,

starting with concepts from kinetic theory. An important difference from classical kinetic theory occurs because inelasticity of collisions between macroscopic particles and the consequent dissipation of energy must be represented by appropriate models. Furthermore, the interstitial gas exerts drag on the particles, leading to interaction terms in the averaged transport equations. One especially notable component of the theory is the concept of granular temperature, which represents the mean kinetic energy associated with fluctuations in the velocities of the particles.

The resulting model equations describe the dynamics in terms of the conservation of mass, momentum, and granular temperature for each species of particles. These equations can describe the independent accelerations of, and the exchanges of momentum and energy among, the particle species. The equations for the particle species are closed by providing a separate Gaussian distribution of velocity for each particle species; this provision is valid as long as gradients of the mean variables are small and the particles behave approximately as nearly elastic hard spheres. In the regions of very high solids volume fractions, the stress tensor is augmented by a frictional-transfer submodel of stress vs. strain.

The model has been applied in several test cases: (1) predictions of the shear and normal stresses in homogeneous shear flows, (2) simulations of the particle pressure along the wall of a bubbling bed, and (3) a comparison between simulations of monodisperse and binary mixtures in a homogeneously aerated bed. For cases for which experimental data were available, the results of the simulations were found to approximate the data reasonably well (for example, see figure).

This work was done by Josette Bellan and Danny Lathouwers of Caltech for **NASA's Jet Propulsion Laboratory**. *Further information is contained in a TSP [see page 1].*
NPO-20937

Making Three-Dimensional Holograms Visible From All Sides

Three-dimensional virtual reality displays could be viewed without visual aids.

NASA's Jet Propulsion Laboratory, Pasadena, California

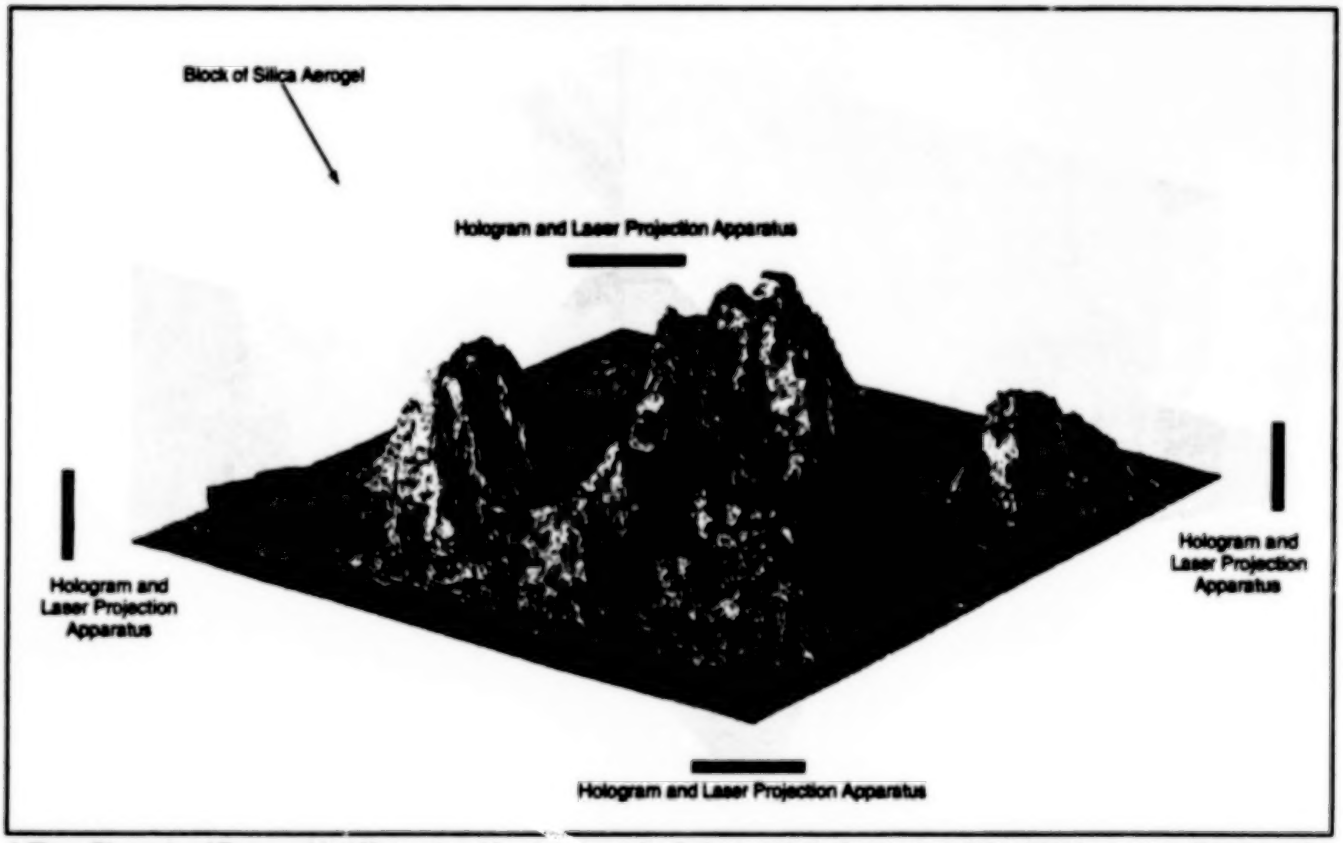
Block of Silica Aerogel
Hologram and Laser Projection Apparatus
Hologram and Laser Projection Apparatus
Hologram and Laser Projection Apparatus
Hologram and Laser Projection Apparatus

A Three-Dimensional Topographical Map, projected from holograms for display in a block of aerogel, would be visible from any position above the projection table. One of the holograms could be generated by a computer to depict a vehicle moving on the terrain.

A technique for projecting holographic images to make both still and moving three-dimensional displays is undergoing development. Unlike older techniques based on stereoscopy to give the appearance of three-dimensionality, the developmental technique would not involve the use of polarizing goggles, goggles equipped with miniature video cameras, or other visual aids. Unlike in holographic display as practiced until now, visibility of the image would not be restricted to a narrow range of directions about a specified line of sight to a holographic projection plate. Instead, the image would be visible from any side or from the top; that is, from any position with a clear line of sight to the projection apparatus. In other words, the display could be viewed as though it were an ordinary three-dimensional object. The technique has obvious potential value for the entertainment industry, and for military uses like displaying battlefield scenes overlaid on three-dimensional terrain maps.

An essential element of the technique is the use of block of silica aerogel as the display medium. Silica aerogel is an open-cell glass foam with a chemical composition similar to that of quartz and a density as low as about one-tenth that of quartz. The sizes of cell features are of the order of 100 Å. Silica aerogel is a suitable display medium because it is nearly completely transparent, with just enough scattering and reflection to enable the generation of a real image.

The figure illustrates a conceptual application in which a three-dimensional topographical map would be displayed by fusing images projected into a block of silica aerogel from four separate holograms. One could use static holograms to project still images, either alone or in combination with computer-generated holograms to project moving or still images. A computer-generated hologram would be downloaded into a large liquid-crystal, which would be illuminated by a laser projection apparatus to display the holographic image in the aerogel block. For example, the terrain image could be projected from static holograms, while a computer-generated hologram would be used to depict a vehicle moving on the terrain.

This work was done by Frederick Mintz, Tien-Hsin Chao, Peter Tsou, and Nevin Bryant of Caltech for **NASA's Jet Propulsion Laboratory**. *Further information is contained in a TSP [see page 1].*

This invention is owned by NASA, and a patent application has been filed. Inquiries concerning nonexclusive or exclusive license for its commercial development should be addressed to the Patent Counsel, NASA Management Office–JPL [see page 1]. Refer to NPO-20101.

Multiple-Path-Length Optical Absorbance Cell

Wide dynamic range is provided for measuring widely different concentrations of CDOM.

Stennis Space Center, Mississippi

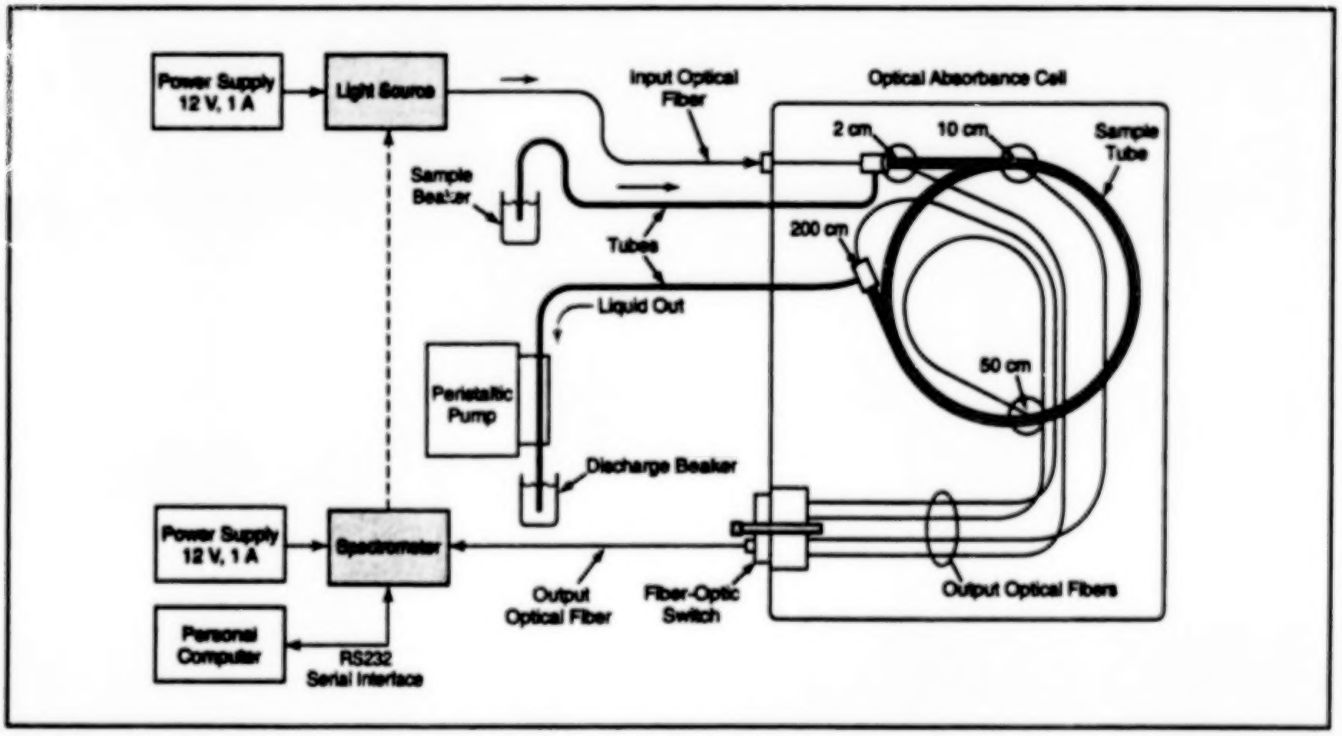

The Optical Absorbance Cell of this instrument is a liquid-core waveguide that includes fiber-optic taps for measuring absorption over several different path lengths.

An optical absorbance cell that offers a selection of multiple optical path lengths has been developed as part of a portable spectrometric instrument that measures absorption spectra of small samples of water and that costs less than does a conventional, non-portable laboratory spectrometer. The instrument is intended, more specifically, for use in studying colored dissolved organic matter (CDOM) in seawater, especially in coastal regions. Accurate characterization of CDOM is necessary for building bio-optical mathematical models of seawater. The multiple path lengths of the absorption cell afford a wide range of sensitivity needed for measuring the optical absorbances associated with the wide range of concentrations of CDOM observed in nature.

The instrument operates in the wavelength range of 370 to 725 nm. The major subsystems of the instrument (see figure) include a color-balanced light source; the absorption cell; a peristaltic pump; a high-precision, low-noise fiber optic spectrometer; and a laptop or other personal computer. A fiber-optic cable transmits light from the source to the absorption cell. Other optical fibers transmit light from the absorption cell to the spectrometer, as described below.

The absorption cell is of a type known in the art as a liquid-core waveguide: the liquid to be characterized is contained in a narrow tube. The material of the tube or a material coating the outside of the tube is chosen to be of an index of refraction less than that of the liquid so that light propagating inside the liquid remains confined by total internal reflection. Thus, the liquid and tube constitute an optical waveguide or optical fiber.

The tube has an inner diameter of 2 mm and is coiled for compactness. The peristaltic pump draws the sample water from a beaker into and along the tube and discharges the water into another beaker.

Light that has propagated through the liquid in the tube is collected by an optical fiber at path lengths of 2, 10, 50, and 200 cm from the light-input end. By means of a fiber-optic switch, the light from one of these optical path lengths is selected for transmission to the spectrometer via a fiber-optic cable. The spectrometer readings are transmitted to the computer for analysis.

In tests using phenol red secondary standards, the instrument exhibited a baseline repeatability in absorbance of better than 1 mAU. During absorption measurements of natural CDOM samples, the instrument exhibited a sensitivity of about 0.002 m^{-1} at a wavelength of 370 nm. On the other hand, it was found that by using the 2-cm path length cell, one could measure CDOM absorbance as high as 200 m^{-1} at 370 nm. Hence, the instrument has an exceptional dynamic range, as needed to measure a wide range of CDOM concentrations.

This work was done by Richard L. Miller of **Stennis Space Center** *and Mathias Belz and Su Yi Liu of World Precision Instruments Inc.*

In accordance with Public Law 96-517, the contractor has elected to retain title to this invention. Inquiries concerning rights for its commercial use should be addressed to

World Precision Instruments Inc.
175 Sarasota Center Boulevard
Sarasota, FL 34240

Refer to SSC-00143, volume and number of this NASA Tech Briefs *issue, and the page number.*

Cold Flow Calorimeter

This apparatus can measure a rapidly varying heat-transfer coefficient.

Marshall Space Flight Center, Alabama

The cold flow calorimeter is an apparatus for measuring a possibly rapidly varying heat-transfer coefficient on a surface. The cold flow calorimeter includes (1) a small strain gauge bonded to a small, thin steel shim that is placed on the surface of interest and (2) a circuit that controls the electric power supplied to the strain gauge to keep the strain-gauge grid at a constant temperature [e.g., 150 °F (=66 °C)]. The instantaneous value of the heat-transfer coefficient is deduced from the instantaneous power required to maintain the constant temperature. The heat-transfer coefficient measurable by use of this apparatus can range from values characteristic of natural convection to values as large as about 1,000 Btu/(ft·h·°R) [=1.7 kW/(m·K)].

In the original application for which this apparatus was conceived, there is a need to measure heat-transfer coefficients along an O-ring surface in a nozzle joint in a solid-fuel rocket motor. In this application, there is a gas path to the sealing O ring. The cold flow calorimeter makes it possible to determine the coefficient of transfer of heat from a confined gas jet to the sealing O ring. The measurement data obtained by use of the cold flow calorimeter can be used to verify solutions from computational fluid dynamics, determine spreading factors, and increase the accuracy of predictions of the transfer of heat to an O ring to which there is a confined gas path.

This work was done by Ed Mathias and John Shipley of Thiokol Corp. for **Marshall Space Flight Center.** *For additional information, please contact Thiokol Corp. at (435) 863-2268.*

MFS-31463

Infrared CO_2 Sensor With Built-In Calibration Chambers

A proposed infrared CO_2 sensor, operated in conjunction with suitable readout, data-processing, and control circuitry, could be calibrated repeatedly during operation to compensate for changes in sensor response induced by such phenomena as aging and changes in temperature. The sensor would include an infrared source, an infrared detector, and four chambers containing CO_2 at various concentrations. Three of the chambers would be calibration chambers: they would be sealed and would contain CO_2 at known low, intermediate, and high concentrations, respectively. The fourth chamber would be filled with the gas under test containing CO_2 at a concentration to be determined. There would be optics for multiplexing infrared radiation from the source through the four chambers and demultiplexing the radiation from the chambers to the infrared detector. During an operation/calibration cycle, radiation would be directed through each chamber in turn, and the response of the detector recorded for each chamber. A three-point calibration for that cycle would be computed from the responses for the three calibration chambers. Then the concentration of CO_2 in the fourth chamber would be computed by simply multiplying the detector response for that chamber by a factor calculated as part of the calibration.

This work was done by Jose M. Perotti and Gregory A. Hall of **Kennedy Space Center.** *Further information is contained in a TSP [see page 1].*

KSC-12177

Solid-State Potentiometric CO Sensor

A solid-state sensor was developed that measures the concentrations of one or more gases of interest in a mixture of gases. This simple solid-state sensor produces a voltage signal that is sensitive to CO concentration from percent to ppm (parts per million) levels. It was intended originally for use in measuring concentrations of carbon monoxide in fuel and oxidizer gases generated on Mars in a process that would include the decomposition of atmospheric CO_2 into CO and O_2. In that application, the sensor would be capable of measuring high concentrations of CO expected to occur on the fuel side of the process, yet would be selective and sensitive enough to measure the low concentrations of CO in O_2 expected on the oxidizer side of the process. On Earth, sensors like this one could be used to detect toxic concentrations of CO emitted in diverse processes, including refining of petroleum and combustion of hydrocarbon fuels in furnaces and automobiles.

This work was done by Eric D. Wachsman and Abdul-Majeed Azad of the University of Florida for **Kennedy Space Center.**

KSC-12256

Characteristics of Supercritical Transitional Mixing Layers

This report describes a study of three-dimensional, temporal mixing layers between different fluids initially flowing at different velocities under supercritical conditions. The study involved direct numerical simulations by use of a validated mathematical model of high-pressure-fluid behavior that has been described in a number of prior *NASA Tech Briefs* articles. In some cases, the fluids were heptane and nitrogen; in other cases, they were hydrogen and oxygen. In all these simulations, the mixing layers underwent transition to turbulence. In the simulations, the mixing was excited by perturbations at various wavelengths. Analysis of the simulation results showed that all layers developed convoluted regions of high density-gradient magnitude (HDGM), resulting from both distortion of initial density boundaries and from mixing. Species mass fractions in the HDGM regions were found to depend weakly on the perturbation wavelength. Evaluation of a method that involves the use of assumed probability density functions (PDFs) for describing supercritical transitional flows revealed that two PDFs commonly used in this method are inappropriate for representing a conserved scalar, and that the PDFs of the partial density and temperature of the two fluids are correlated, so that a model of a reaction rate, which is a joint PDF, as a product of marginal PDFs is invalid.

This work was done by Josette Bellan and Nora Okong'o of Caltech for **NASA's Jet Propulsion Laboratory**. *To obtain a copy of the report, "Characteristics of Supercritical Transitional Temporal Mixing Layers," see TSP's [page 1].*

NPO-30292

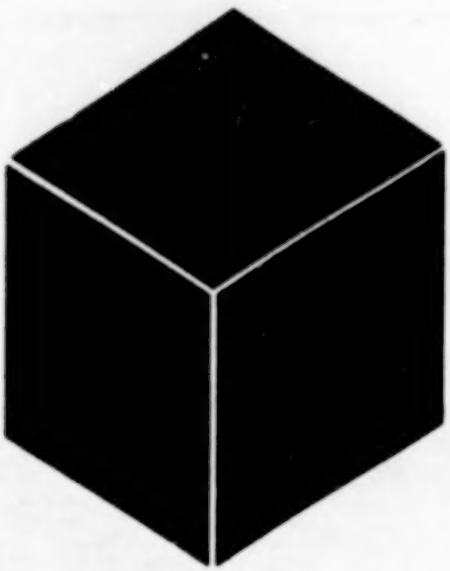

Materials

Hardware, Techniques, and Processes

27 Flat Membrane Device for Dehumidification of Air

BLANK PAGE

Flat Membrane Device for Dehumidification of Air

Water vapor is not condensed; instead, it is transported to vacuum.

Lyndon B. Johnson Space Center, Houston, Texas

A device based on the transport of water through a membrane to a vacuum has been developed for dehumidifying a stream of air in the life-support system of a spacecraft or space suit. The device could also be adapted to terrestrial use in dehumidification of air in an air-conditioning stream or drying of air or another gas in a chemical processing stream. The design of this device is an advance in that it decreases (relative to prior designs) the weight, power consumption, and volume of the dehumidifier in the life-support system or other gas-circulation system in which the device is used. In the case of a spacecraft or space suit, the design thereby also increases safety and health margins. Although the membranes in the device must be replaced periodically and a vacuum source is essential for its operation, no other dehumidifier works as well in a spacecraft or space suit.

Unless controlled, the concentrations of CO_2 and H_2O in respirable air in a spacecraft or space suit quickly reach unacceptably high levels. Heretofore, life-support systems in spacecraft and space suits have included solid metal hydroxides for depleting exhaled CO_2, and condensers integrated with cooling sources for removing excess moisture. To enable the condensers to function, such systems must also include microgravitational phase separators and coolant/heat sink subsystems, all of which contribute to weight, volume, and consumption of power.

The present device operates without need for either a coolant/heat sink subsystem or a microgravitational phase separator. Moreover, in the original outer space application, the vacuum needed for operation is available naturally, so that it is not necessary to incur the cost, weight, and power penalty of a vacuum source. Hence, in comparison with breathing air systems of prior design, it is possible to simplify breathing loop interfaces, reduce weight and volume, and decrease the amount of power expended, thereby also saving on the cost of fuel.

The device contains one or more modules in which spaces in a vent-layer assembly alternate with spaces in a vacuum-layer assembly and the vent and vacuum spaces are separated by flat sheets of a polyelectric membrane material that is permeable by water (see figure). The vent-layer assembly includes a vent frame, a metal foam insert, and screens. The frame is rectangular and is sized to optimize the pressure drop characteristics of the vent-gas and water-vapor flows. The metal foam insert is bonded to the top and bottom of the frame and sandwiched between a pair of screens that provide additional support so that the membrane is not torn against the surface of the metal foam. Flow holes connect the central section of the frame to header slots and allow humid gas to enter the frame without leaking into the vacuum space. Dovetailed O rings grooved to fit the perimeter of the frame retain a gasket during assembly of the module. The thickness of the vent layer is chosen to be the minimum thickness needed to maintain top and bottom gasket seals.

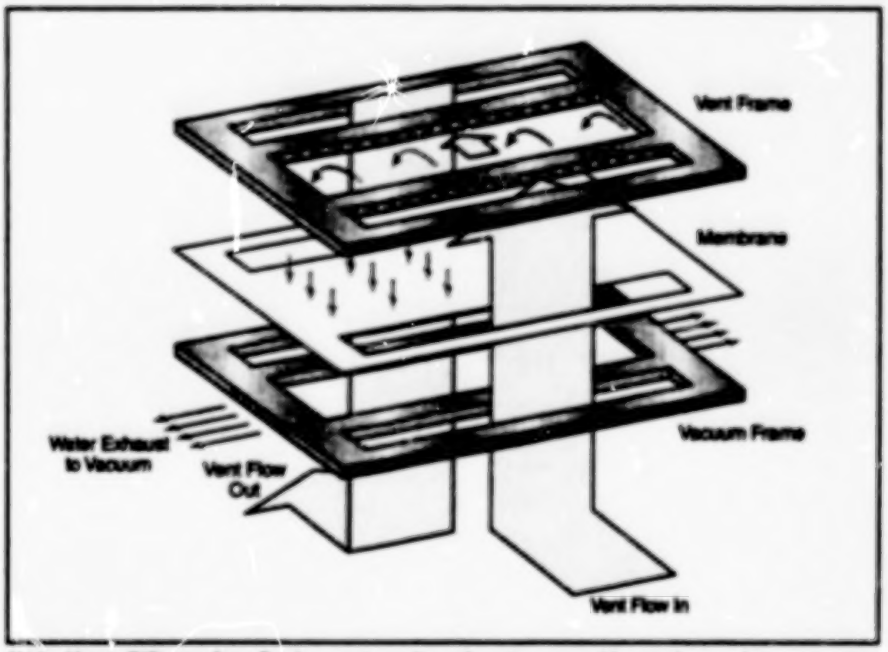

Water Vapor Diffuses from flowing vent gas through water permeable membranes into a vacuum.

The vacuum-layer assembly is similar to the vent-layer assembly except that its flow holes are on the short ends and there is no header for a vacuum-layer, eliminating the need for another set of gaskets on each layer. Inasmuch as the flow of water vapor is a fraction (typically 4 percent by volume) of the flow of the gas to be dehumidified (hereafter called vent gas for short), the vacuum frame can be made thinner than the vent frame to minimize overall volume. This frame is so thin that a single gasket, held in place by a retaining ring, seals against layers above and below the vent layers. The number and size of vacuum holes satisfy two constraints: (1) the minimum equivalent area limits the back pressure of vapor; and (2) the maximum equivalent area restricts the vent flow if one or more membranes rupture. Top and bottom end plates, sized to provide sufficient stiffness, apply an even pressure to the gaskets to prevent leakage. These plates also include ports through which the vent gas flows into and out of the module, plus ports for testing the vent gas.

Modules like the one described above are stacked in alternating layers, beginning and ending with a vacuum frame. The modular nature of the device provides flexibility for changing the membrane area to satisfying requirements for the conditions of a particular application.

This work was done by Karen Murdoch and C. H. Miller of United Technologies for **Johnson Space Center.**
MSC-22878

BLANK PAGE

Computer Programs

Electronic Components and Circuits

31 Firmware for a Small Motion-Control Processor

Materials

31 Advanced Fatigue-Crack-Growth and Fracture-Mechanics Program

Mathematics and Information Sciences

31 Software for Sequencing Spacecraft Actions

32 Program Distributes and Tracks Organizational Memoranda

BLANK PAGE

Electronic Components and Circuits

Firmware for a Small Motion-Control Processor

A C-language computer program implemented as firmware controls the operations of a microprocessor on a 3-by-1-inch (approximately 76-by-25-mm) motion-control circuit board denoted a widget board. The firmware implements a serial communication interface according to the inter integrated circuit bus (I^2C) standard by use of an interrupt-driven state machine to enable communication to occur during execution of commands. The firmware also controls the operation of a motion-control integrated-circuit chip, a serial analog-to-digital converter, a serial digital-to-analog converter, and the digital input/output lines of the microprocessor. The digital input/output control portion of the firmware offers a masking capability. The firmware includes a provision for dynamically downloading, to the widget board, of a small program (limited to 12 lines and to 256 bytes). A microexecutive program executes the downloaded program in a loop, with the option of continuous looping. The execution of the downloaded subprogram can be interrupted at the user's request. The widget firmware includes a set of more than 48 commands, 24 control operations, and 24 query operations.

This program was written by Issa Nesnas of Caltech for **NASA's Jet Propulsion Laboratory.** *Further information is contained in a TSP [see page 1].*
NPO-30243

Materials

Advanced Fatigue-Crack-Growth and Fracture-Mechanics Program

The NASGRO 3.0 computer program is an advanced version of a program used by NASA and the European Space Agency for fracture-control analysis of space-system structures and other hardware. The prior version, NASA/FLAGRO 2.0, was described in "Updated Fatigue-Crack-Growth and Fracture-Mechanics Software" (MSC-22550), *NASA Tech Briefs*, Vol. 19, No. 12 (December 1995), page 74. NASGRO 3.0 affords additional capability for durability and damage-tolerance analysis of aircraft structures and other mechanical systems. Because this code offers state-of-the-art and general capabilities in fracture mechanics and crack-propagation analysis, its usefulness extends beyond aerospace to numerous industrial applications. For example, it can provide guidance for prevention of catastrophic failures that originate in crack-like flaws in offshore oil structures, pressure vessels, pipes, diesel engines, and railroad tank cars. The program is also useful as an instructional device for courses in fatigue and fracture mechanics.

The objective in developing NASGRO 3.0 was to extend NASA/FLAGRO 2.0 (which was released in 1994) to accommodate more recent advancements in fracture mechanics and crack-propagation theory, to meet needs for damage-tolerance and durability analysis of aircraft, and to enable the program to function within the Windows 95/98, Windows NT, and Unix operating systems. The changes made in pursuit of this objective were the following:

- A graphical user interface (GUI) was developed to make input of data easier and more intuitive.
- Load-interactive or retardation routines were added to account for changes in crack-growth rates due to fatigue spectrum (nonconstant) loading. Five different mathematical models have been included: the generalized Willenborg, the modified generalized Willenborg, the Walker-Chang-Willenborg, the strip-yield, and the constant-closure models.
- New and improved crack solutions were added for cases of bolts, cracks from holes, and nonlinear stress distributions.
- Spectrum-input routines have been improved to provide more flexibility in the use of pre-existing spectrum files.
- A materials database has been added, along with a GUI that gives users access to the data from which the material-property curves are derived. A software module called "NASMAT" contains a base of experimental data that are available for easy access, viewing, and use in deriving crack-growth material constants required for safe-life analysis.
- The threshold equation has been improved by incorporation of a newer, more accurate mathematical model of fatigue-crack-growth thresholds.

This program was written by Royce G. Forman of **Johnson Space Center;** *V. Shivakumar, Sambi Mettu, Joachim Beek, and Feng Yeh of Lockheed Martin; and Leonard Williams of GB Tech, Inc., and is available at http://mmptdpublic.jsc.nasa.gov/nasgro/nasgromain.html.*
MSC-23082

Mathematics and Information Sciences

Software for Sequencing Spacecraft Actions

SEQ_GEN is a component of the Sequence Subsystem computer program, which assists in generating a sequence of commands to be executed by a control computer aboard a spacecraft to perform scientific observations and supporting engineering actions in response to requests by numerous users. SEQ_GEN assists a designer in devising a final, valid sequence. Using SEQ_GEN, the designer prepares a file of requested spacecraft actions. SEQ_GEN then processes this file plus a file of spacecraft- and mission-specific information prepared by another Sequence Subsystem software component to (1) generate the sequence of commands, (2) predict what the commands will cause to happen on the spacecraft, and (3) give warnings when the sequence violates rules or causes misuse of spacecraft systems. SEQ_GEN generates an interactive graphical time-line display of the predictions and warnings. The user can change the sequence by keyboard entry in a text file, or by use of a mouse to add or delete an item or move an item to a new position on the display. SEQ_GEN then processes the revised input data, starting from a time earlier than the earliest time affected by the change(s). The process is repeated, if necessary, until a valid sequence is produced.

This program was written by Russell M. Bell, Dang Le, Imin Lin, Winthrop Lombard II, Robert Oliphant, Tallun O'Reilly, Jose J. Salcedo, and Thomas W. Starbird of Caltech for **NASA's Jet Propulsion Laboratory.** *Further information is contained in a TSP [see page 1].*

This software is available for commercial licensing. Please contact Don Hart of the California Institute of Technology at (818) 393-3425. Refer to NPO-20452.

Program Distributes and Tracks Organizational Memoranda

Closed Loop Accounting Management System (CLAMS) is a computer program for Web-based distribution and tracking of memoranda within an organization. An item for distribution is entered by a user who has administrative access. The item is assigned to affected users, to whom e-mail messages are sent. Upon receipt of such an e-mail message, a user gains access to an "open items" page from a link within the message. From the "open items" page, the user can (1) link to the item, (2) select a "notes" button to leave a reminder about the item, or (3) select a "close" button to close the item, indicating that the user has received and understands the item. CLAMS can be used to effect the automated distribution of new and updated items to users on predetermined lists. CLAMS enables managers to track the statuses of users and distributed items: For a given item, CLAMS can tell (1) who has it open and for how long and (2) who closed it and when; regarding a given user, CLAMS can tell (1) which items the user has open and for how long and (2) which items the user closed and when.

This program was written by Mike Olejarski of United Space Alliance for **Kennedy Space Center**. *Further information is contained in a TSP [see page 1].*
KSC-12289

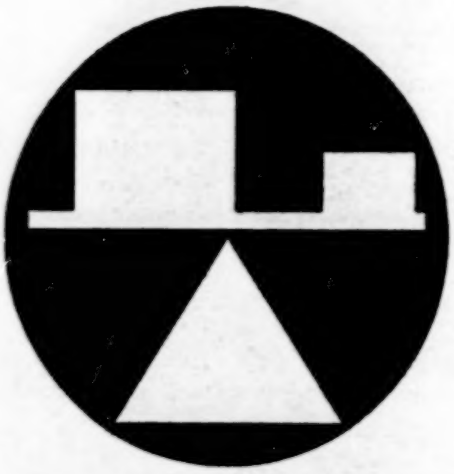

Mechanics

Hardware, Techniques, and Processes

35 Inverted Hindle Mount Reduces Sag of a Large, Precise Mirror
36 Gear Bearings and Gear-Bearing Transmissions
37 Heart-Pump-Outlet/Cannula Coupling

BLANK PAGE

Inverted Hindle Mount Reduces Sag of a Large, Precise Mirror

The mirror is suspended from above by multiple, equally loaded supports.

Goddard Space Flight Center, Greenbelt, Maryland

A mount has been devised to satisfy a requirement to suspend a highly precise, flat, circular, low-thermal-expansion glass mirror in a horizontal plane with its reflective side down while keeping the reflective mirror surface flat to within a peak-to-valley depth of less 50 nm. The difficulty of the suspension problem and the significance of the mount conceived as the solution of the problem arise from the large size and weight of the mirror (diameter 101.7 cm, thickness 18.8 cm, mass 385 kg).

The mount is an inverted version of the Hindle mount, which was first published in 1945 and is named after its inventor (Dr. J. H. Hindle). The Hindle mount supports a flat, circular mirror on multiple pads that are located so that all of the pads bear the same proportion of the total weight and the sag of the mirror under its own weight between the supports is minimized. The number of support pads in a Hindle mount is an integer multiple of three. The sag can be reduced by increasing the number of support pads. The present mount is based on a Hindle-mount geometry of nine support points grouped into three triangles (see Figure 1).

The original Hindle-mount concept applies to a mirror suspended from its lower face with its reflective side up; the weight of the mirror presses it against the support pads, and the resulting friction often suffices to hold the mirror in place on the pads. In the present inverted Hindle mount, the mirror is suspended from its upper face; consequently, the weight of the mirror tends to pull it away from its supports, making it necessary to fasten the mirror to the supports in some fashion.

Figure 2 depicts some parts of the present inverted Hindle mount. The nine supports are made of Invar — a low-thermal-expansion Fe/Ni alloy. To distinguish them from the compression-loaded support pads of a traditional Hindle mount, these tensile-loaded supports are called "anchors." The lower end of each anchor has an area of 3 in.^{2} (≈19.4 cm^2) and is bonded to the to face of the mirror by use of 3M's 2216 (or equivalent) clear high-performance epoxy. The upper end of each anchor is tapped to accept a bolt. The upper ends of the anchors in each group of three are bolted loosely, with spherical washers, to a triangular aluminum plate 1 in. (2.54 cm) thick. The loose bolting and spherical washers allow some limited rotation and translation, thereby helping to prevent the buildup of bending moments that could cause the anchors to peel away from the mirror surface at the epoxy joints.

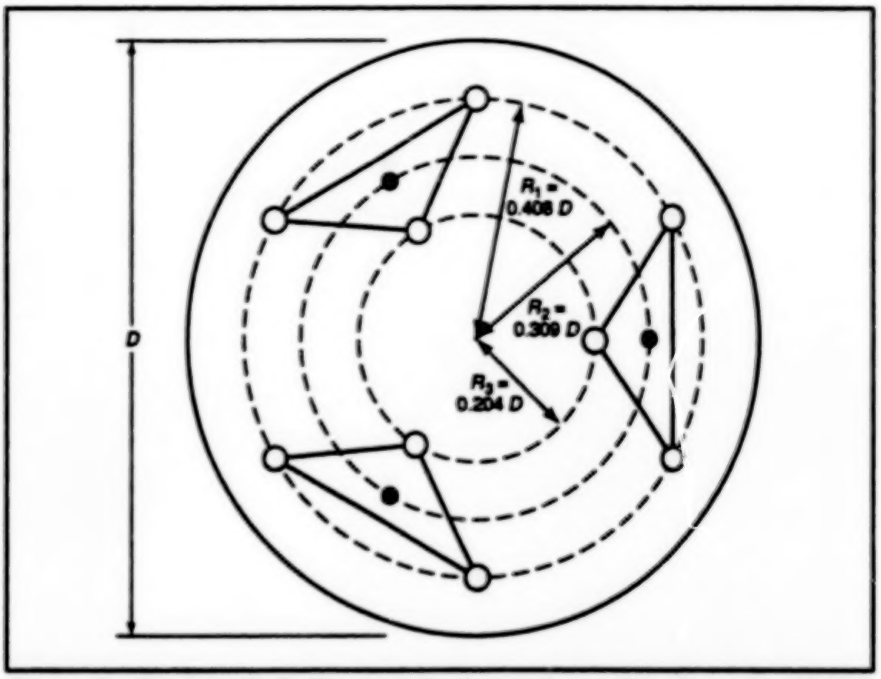

Figure 1. The Nine-Point Hindle Mount includes six supports on a circle with a radius of 0.408*D* and three supports on a circle with a radius of 0.204*D*, where *D* is the outer diameter of the mirror. The supports in each group of three are connected to a triangular plate supported at its centroid, which lies on a circle with radius 0.309*D*. When the three triangular plates are picked up at their centroids, equal weight is borne by all nine supports.

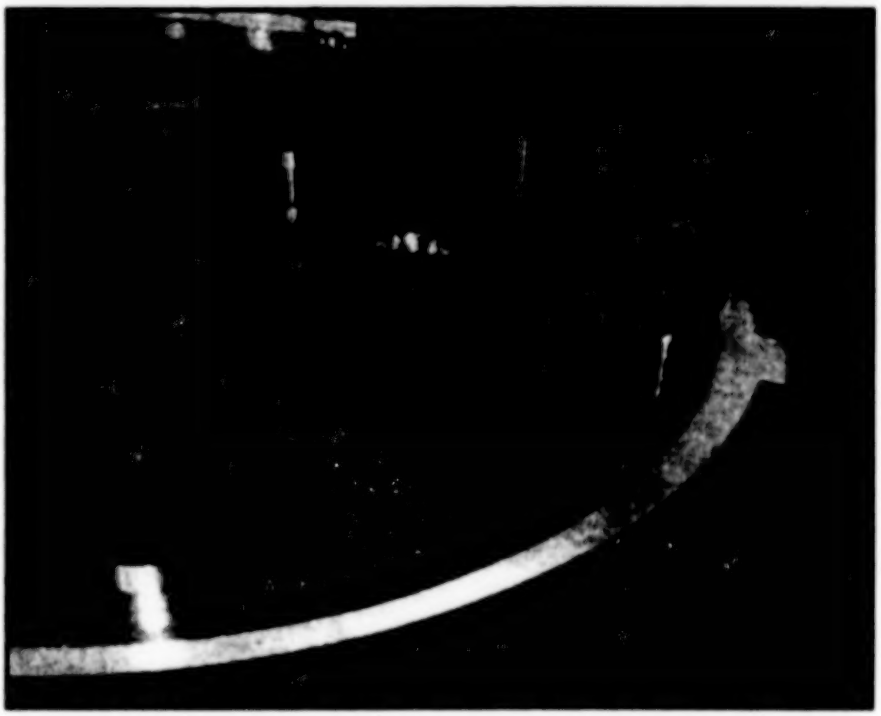

Figure 2. Parts of the Inverted Hindle Mount are attached to an aluminum disk of the same size as (and slightly heavier than) the glass mirror that the mount is intended to support. (The aluminum disk was used during development so as not to risk damage to the expensive glass mirror.)

Each plate is supported from above by means of a clevis/ball-joint coupling

attached to the plate at the centroid of the triangle defined by the three support points. The clevis is, in turn, supported from above by a threaded rod that passes through a massive overhead frame and engages a nut on top of the frame. The freedom of rotation of the clevis/ball joints contributes to the relief of any bending moments that could, if allowed to build up, cause peeling at the epoxy joints.

Experience in the development of the inverted Hindle mount revealed that it can be difficult to form reliable epoxy bonds between the anchors and the top surface of the mirror. Therefore, the mount must be augmented by handling fixtures with safety features to prevent the mirror from falling in the event of failure of one or more epoxy bonds.

This work was done by David W. Robinson of **Goddard Space Flight Center.** *Further information is contained in a TSP [see page 1].*
GSC-14316

Gear Bearings and Gear-Bearing Transmissions

Planetary transmissions could be simpler, cheaper, and more rigid.

Goddard Space Flight Center, Greenbelt, Maryland

Figure 1. A Working Gear-Bearing Transmission shown here has a 70/1 speed reduction in a 1.25-in.-diameter-by-0.75-in. (3.18-cm-diameter-by-1.91-cm) package.

Gear bearings are conceptual mechanical components so named because they function as gears and as roller and/or thrust bearings. Gear bearings will be essential components of the next generation of compact, large-mechanical-advantage gear drives.

Figure 1 shows a working gear-bearing transmission with 70/1 gain in a 1.25-in.-diameter-by-0.75-in. (3.18-cm-diameter-by-1.91-cm) package. Gear bearings exist as spur- or helical-gear variants of two basic types: roller gear bearings and phase-shifted gear bearings. For the sake of brevity, only spur-gear variants are described here; suffice it to say that the principles of operation of the helical-gear variants are similar.

Figure 2(a) depicts selected aspects of roller spur-gear bearings and a partial planetary assembly containing roller spur-gear bearings. The diameter of the roller portion of each roller spur-gear bearing equals the pitch diameter of the spur-gear portion. The gear teeth are crowned at the roller end, such that the apogee of the crown on each tooth lies at the roller diameter/pitch diameter: This arrangement provides thrust-bearing strength as well as matching of speeds and, hence, efficiency.

The planetary assembly would inherently hold itself together, without bracing by other structures. For example, if a planetary roller gear bearing shown in the cross-sectional view were pushed downward, the axial slid-

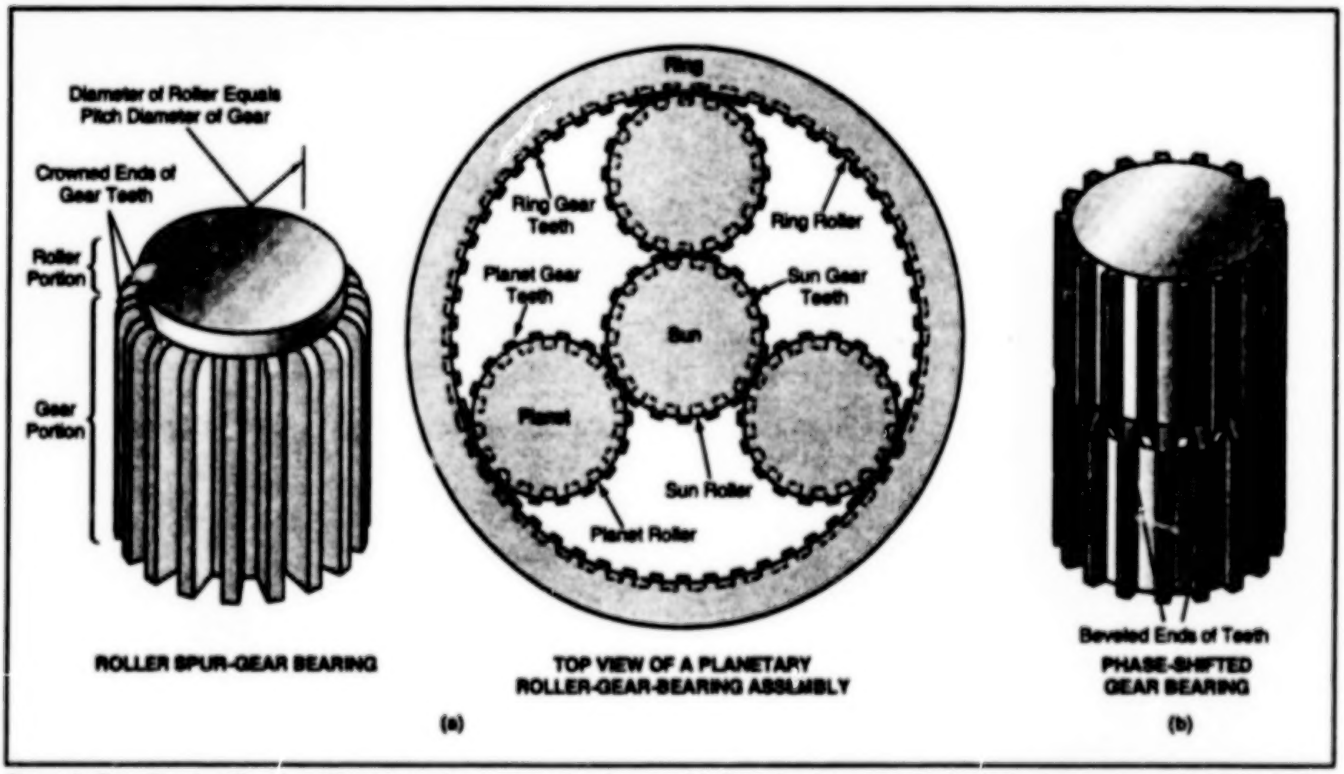

Figure 2. Gear-Bearing Configurations: (a) roller spur-gear bearings would offer advantages, relative to simple spur gears and bearings, for the operation of planetary gear assemblies. (b) A phase-shifted gear bearing could mesh with an identical twin and would offer advantages similar to that of the roller spur-gear bearing depicted in (a).

ing of its teeth with respect to the ring- and sun-gear teeth is stopped by the abutment of the planetary roller against the crowns of the ring-gear teeth. When the same planetary gear is pushed upward, its axial sliding is blocked by abutment of the planetary teeth against the ring roller. Similar interactions prevent axial sliding of the sun roller gear bearing beyond the limits imposed by tooth/roller contacts between the sun and planetary roller gear bearings.

An additional advantage is that by enforcing the desired relative locations of gears more precisely, the incorporation of the rollers increases (relative to simple spur gears) the accuracy of meshing of spur-gear teeth. At the same time, the gears act as highly efficient and precise cages and carriers for the rollers. The net result is a superior, simpler, and relatively inexpensive assembly.

Figure 2(b) presents a simple example of a phase-shifted spur-gear bearing. The teeth in the upper and lower halves are shifted angularly, relative to each other, by precisely a half-tooth interval. This gear bearing meshes with a copy of itself. The upper and lower teeth are beveled and partly interdigitated where they meet. The contact between the beveled surfaces of the upper and lower teeth provide a thrust-bearing capability in a manner similar to that of the contact between the crowns and rollers of the roller gear bearings. Moreover, a planetary assembly containing phase-shifted gears holds itself together in a manner similar to that of an assembly containing roller gear bearings as described above.

This work was done by John M. Vranish of **Goddard Space Flight Center.** *Further information is contained in a TSP* *[see page 1].*

This invention is owned by NASA, and a patent application has been filed. Inquiries concerning nonexclusive or exclusive license for its commercial development should be addressed to the Patent Counsel, Goddard Space Flight Center *[see page 1].* *Refer to GSC-14207.*

Heart-Pump-Outlet/Cannula Coupling

This coupling is separable, free of leaks, and configured to minimize clotting.

Lyndon B. Johnson Space Center, Houston, Texas

A fluid coupling has been developed for use in securing a vascular outflow graft (cannula) to the outlet of a surgically implanted NASA/DeBakey heart-assist pump. The design of the coupling can also be adapted to other applications in which it is necessary to join flexible tubes with rigid ones. A joint formed by use of this coupling is separable, yet free of leaks; this is advantageous in that (1) it is necessary to be able to install or remove a pump in accordance with requirements for surgery, sterilization, and pump maintenance, but (2) seepage of blood from an installed pump/cannula joint cannot be tolerated. Moreover, the coupling provides a smooth transition for flow from the pump outlet to the cannula; this feature helps to prevent clotting, which is triggered by flow-surface discontinuities.

The coupling (see figure) includes tapered and threaded surfaces on the pump outlet tube, a differentially tapered locking collet, a connector nut that mates with the thread on the pump outlet tube, and the affected end portion of the cannula. A volume is provided at the upstream end of the tapered outlet-tube surface to allow excess cannula material (including material extruded by the clamping described below) to expand to form a bulbous collar that helps to retain the cannula in place. This volume also facilitates manufacture and assembly, inasmuch as it desensitizes the joint to slight variations in cannula geometry.

The differential angle between the tapered surfaces of the pump outlet and the locking collet helps to clamp the cannula in place and to provide a seal when the connector nut is tightened. The radial clearance between the locking collet and the connector nut is sufficient to allow the collet to move slightly to align itself for uniform clamping of the cannula. The nut can be tightened to obtain the desired clamping and sealing force, or can be loosened to disconnect the pump from the cannula.

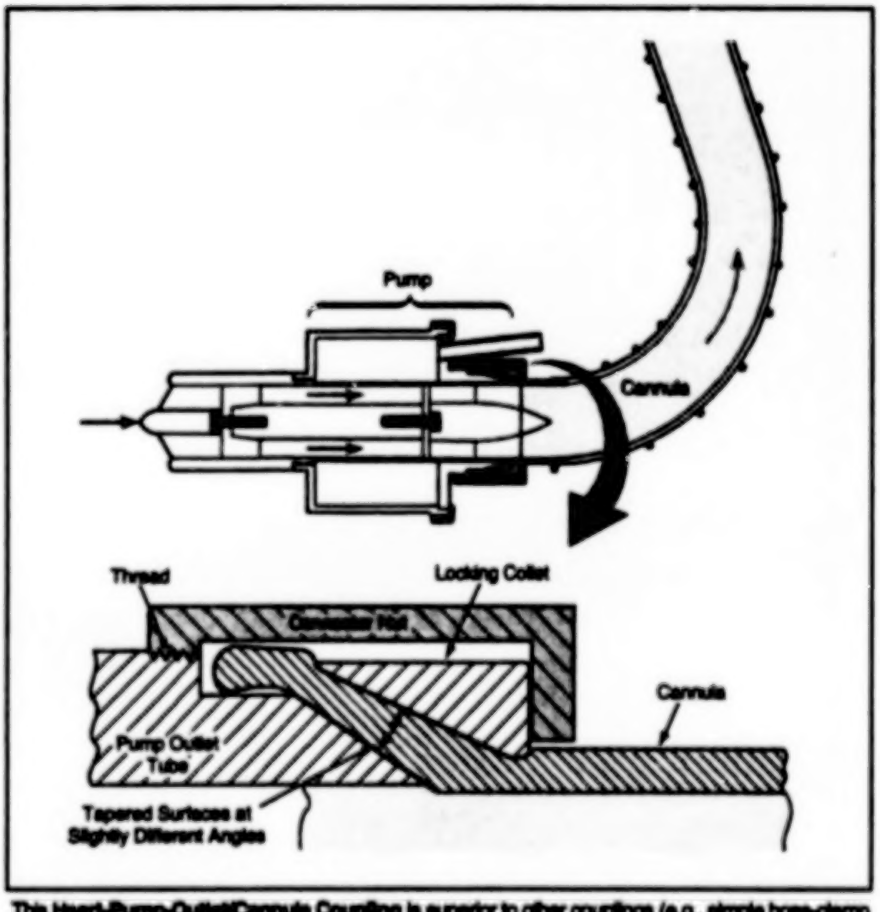

This Heart-Pump-Outlet/Cannula Coupling is superior to other couplings (e.g., simple hose-clamp couplings) that were not designed for coupling heart pumps.

This work was done by Bernard J. Rosenbaum of **Johnson Space Center.** *Further information is contained in a TSP* *[see page 1].*

This invention has been patented by NASA (U.S. Patent No. 6,050,987). Inquiries concerning nonexclusive or exclusive license for its commercial development should be addressed to the Patent Counsel, Ames Research Center, (650) 604-5104. Refer to MSC-22665.

BLANK PAGE

Machinery

Hardware, Techniques, and Processes

41 Surface-Launched Explorers for Reconnaissance/Scouting
42 Magnetically Suspended Optical Chopper Wheel
43 Mesoscopic Steerable Mirror
43 Linear Dynamometer With Variable Stroke and Frequency

Books and Reports

44 Design Concepts for the ISS TransHab Module

BLANK PAGE

Surface-Launched Explorers for Reconnaissance/Scouting

Efficiency of robotic exploration would be increased.

NASA's Jet Propulsion Laboratory, Pasadena, California

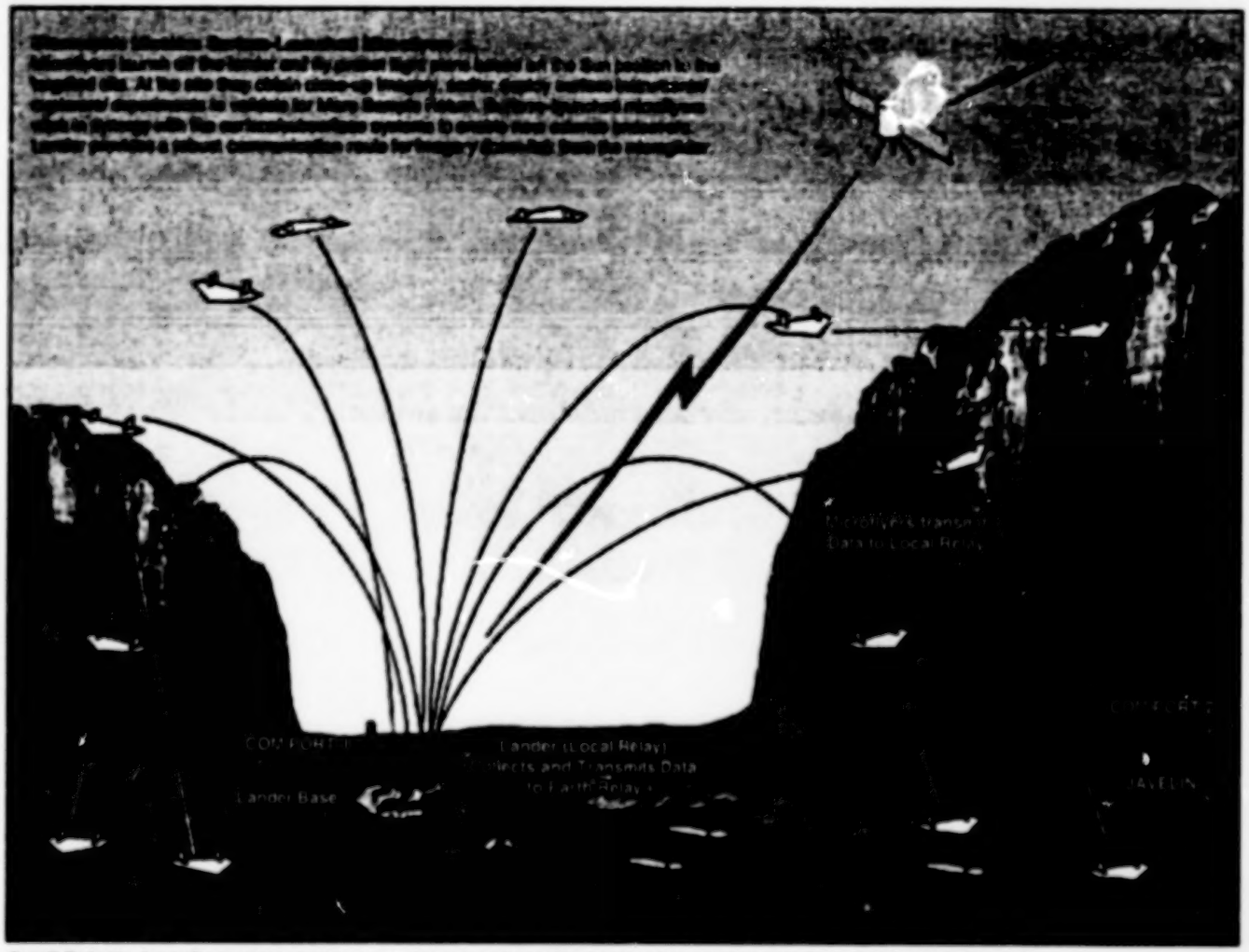

Small Robotic Aircraft would transmit images of terrain and possibly sensory data to an exploratory robotic vehicle (lander).

Small, instrumented, expendable robotic aircraft and projectiles have been proposed for use in scouting for targeted new sites by providing closeup images with ~10-cm resolution, covering large distances ~1 to 10 km quickly and allowing reconnaissance to enable sample return. Denoted microflyers or surface-launched explorers (SLEs), the proposed robotic aircraft and projectiles were conceived especially for use in the exploration of Mars and possibly other distant planets. SLEs could also be adapted to such terrestrial uses as military reconnaissance, exploration of hostile terrain (e.g., volcanoes, steep cliffs, or glaciers), surveying hazardous-waste sites, and searching for victims of earthquakes.

This class of SLEs enables biomorphic missions — hybrid missions which utilize surface assets and aerial assets synergistically to achieve new scientific endeavors along with deploying biomorphic explorers. Biomorphic explorers and related concepts have been described in several previous articles in *NASA Tech Briefs*, the most relevant being "Biomorphic Explorers" (NPO-20142), Vol. 22, No. 9, (September 1998), page 71; "Earthwormlike Exploratory Robots" (NPO-20266), Vol. 22, No. 6, (June 1998), page 11b; "Insectile and Vermiform Exploratory Robots" (NPO-20381), Vol. 23, No. 11, (November 1999), page 61; "Biomorphic Gliders" (NPO-20677), Vol. 25, No. 4 (April 2001); and "Seed-Wing Flyers for Exploration" (NPO-20676), Vol. 26, No. 1, (January 2002), page 47.

SLEs could include guided projectiles, gliders, electrically powered airplanes and helicopters, and possibly other robotic flyers; specific types, designs, and combinations of SLEs would be tailored to specific applications. In a typical application, the SLEs would be launched from a lander/base station/mobile explorer (see figure) or from a spacecraft, aircraft, or other vehicle that delivered the lander to the exploration site. The means of launching could be as diverse as the SLEs themselves: they could include rockets, balloons, pneumatic devices, or spring mechanisms, for example.

An SLE could carry a small video camera, sensors, and a radio transmitter to send images of the terrain to the lander. The images could help in quickly identifying sites of scientific interest to be explored in more detail and allow identifying hazards and slopes and access the area for its potential for sample return. The images could also be helpful in planning the path of other surface/subsurface explorers across the terrain.

An SLE could be designed to safely land after following a ballistic trajectory in the low gravity of Mars. After landing, the SLE

could continue to function as a scientific instrument: For example, it could analyze surface and/or subsurface soil and use its remaining energy to transmit the analytical data to the lander/mobile explorer. One or more SLEs designed to survive impact would resemble javelins and would be launched in such a way that, like javelins, they would embed themselves in the ground at the far ends of their trajectories; these SLEs would serve as radio beacons to aid navigation by the other SLEs as secondary communication ports in addition to the primary port on the lander. The lander serves as the local relay to send the data back to Earth via the orbit.

This work was done by Sarita Thakoor and Terry Martin of Caltech for **NASA's Jet Propulsion Laboratory**. *Further information is contained in a TSP [see page 1].*
NPO-20871

Magnetically Suspended Optical Chopper Wheel

Magnetic bearings offer long life at high speed, without lubrication or wear problems.

Goddard Space Flight Center, Greenbelt, Maryland

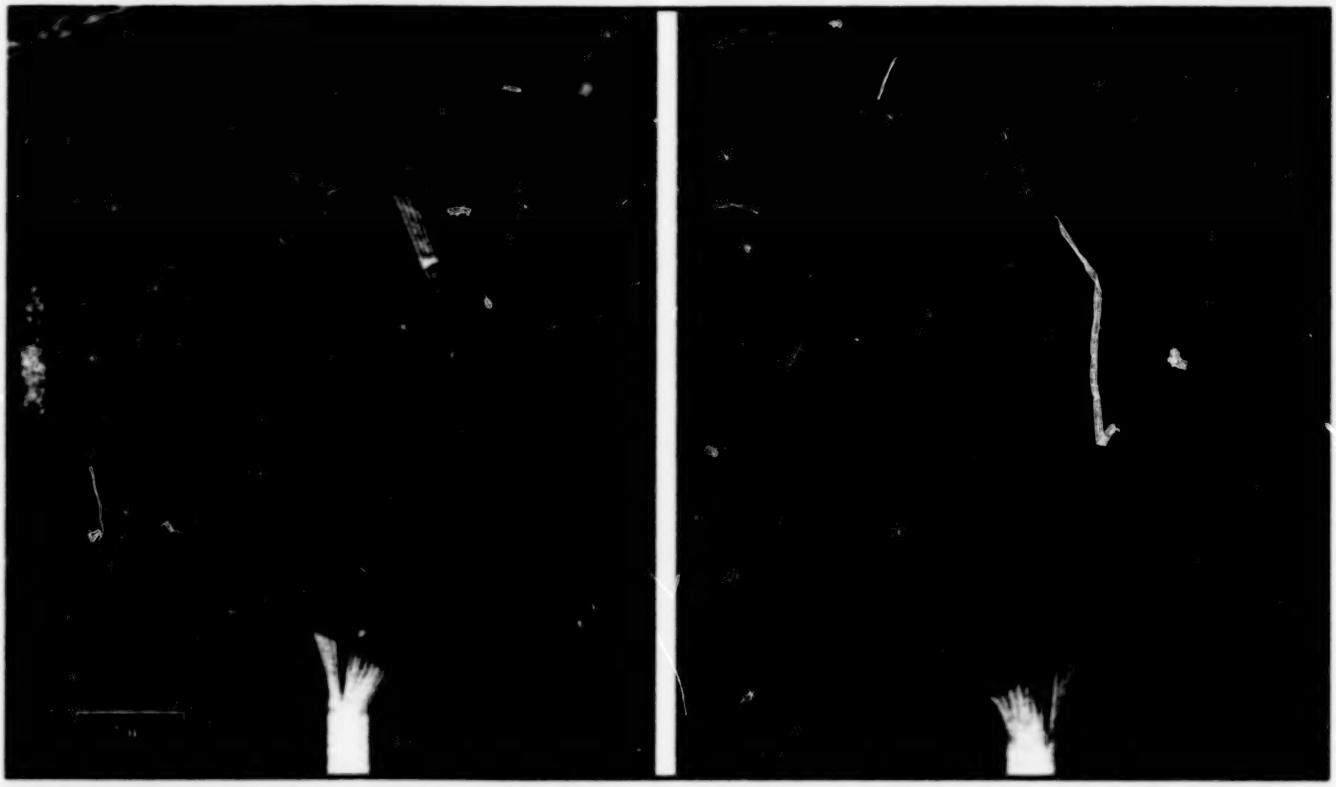

This Optical Chopper Wheel is magnetically suspended, offering certain advantages over traditional light-chopping wheels, which are suspended on ball bearings.

A magnetically suspended, motor-driven light-chopping wheel has been developed as an alternative to a traditional light-chopping wheel suspended on ball bearings. This chopper (see figure) is designed to satisfy application-specific requirements to fit into a small volume, dissipate relatively little power, modulate light with only small errors, and have a long operational life (at least 5 years) at a speed of 5,000 rpm. Relative to ball bearings, the magnetic bearings in this chopper are subject to no wear, and unlike ball bearings, magnetic bearings present no need for lubrication.

This chopper satisfies additional stringent requirements for full redundancy of magnetic-bearing coils, motor coils, and sensors. The magnetic bearings are controlled, in all six degrees of freedom of the chopper wheel, by use of a digital signal processor (DSP) operating in conjunction with sensor and driver electronic circuits. The DSP and the other circuitry are contained on a printed-circuit board with overall dimensions of 6 by 8 in. (≈ 15 by 20 cm).

Unique features of the design and its implementation include the following:

- Homopolar magnetic bearings are made in a novel (patent pending) configuration to minimize rotational losses;
- High-resolution, highly linear optical position sensors with feedback (patent pending) provide automatic gain and offset control;
- An ironless stator motor assembly, optimized to minimize eddy-current losses, is fabricated by use of a modified printed-circuit-board manufacturing technique;
- The DSP is used to compute 6-axis classical and adaptive control algorithms; and
- At the time of reporting the information for this article, this chopper is the smallest known mechanism that incorporates fully active magnetic bearings with full redundancy of electrical components.

This specific application for which this chopper has been developed is an a infrared-sensing instrument aboard an Earth-observing satellite. Magnetic-bearing systems like those of this chopper, but larger, are under consideration for use in diverse outer-space and terrestrial applications in which rotating wheels would be used to store angular momentum and/or kinetic energy.

This work was done by Ken Blumenstock, Carlos Barnaba, Carlos Hernandez, Ken Lee, Joe Schepis, Clarence Johnson, Maurice Lewis, and Paul Haney of **Goddard Space Flight Center**. *Further information is contained in a TSP [see page 1].*
GSC-14323

Mesoscopic Steerable Mirror

This mirror could be slewed rapidly or rotated in small angular increments.

NASA's Jet Propulsion Laboratory, Pasadena, California

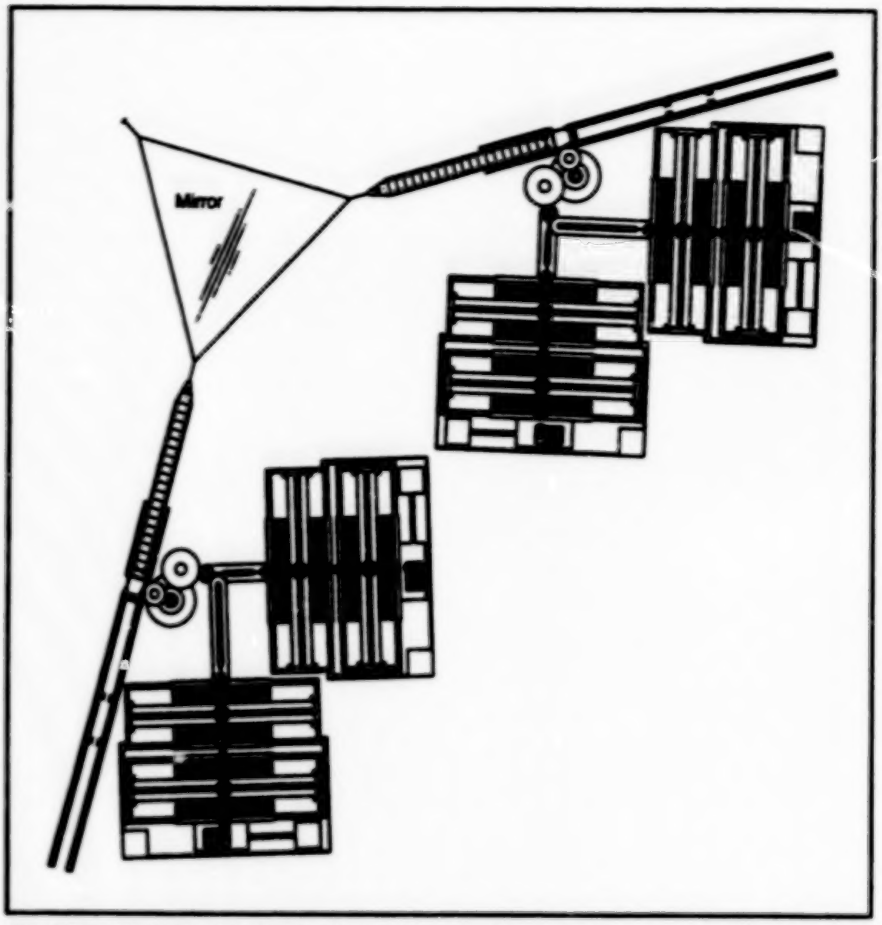

The Mirror Would Be Coupled to micromachined steering mechanisms and supporting structures.

A proposed lightweight, micromachined, multiaxis-steerable mirror would have mesoscopic dimensions. Its steering function would involve mesoscopic positional excursions of its support points and would be characterized by rapid slewing and moderate angular precision.

The mirror, its supporting structures, and its steering mechanisms would be fabricated in a four-layer polycrystalline-silicon surface-micromachining process. The mirror would be triangular and would be supported at its corners. The steering mechanisms and supporting structures connected to two of the corners would include electrostatic comb drives, reduction gear trains, gear-driven translation racks, hinged beams, and flexures (see figure).

In one example design, the electrostatic comb drives would operate in four-phase cycles. For each such cycle, a 19-tooth pinion gear would undergo one revolution. The thrust of each comb drive would be ≈1 μN and could be applied rapidly enough to sustain rotational speeds up about ≈4,000 revolutions per second. Two tandem gear trains would reduce the translation to 1.66 μm per pinion rotation or, equivalently, 0.415 μm per phase step of an electrostatic comb drive, and would increase the torque proportionally.

The triangular mirror would have sides 1.3 mm long. Translation of one corner of the mirror in a 0.415-μm increment as described above would result in a mirror rotation of ≈0.3 milliradian. The flexures would serve as smooth (free of stiction) means of bending and rotational coupling between the corners of the mirror and beams that hold the mirror on a substrate. The flexures could accommodate rotations and bends of at least half a radian. The maximum speed of translation, of a hinged beam would be 6 mm/s, corresponding to a rate of rotation of about a radian per second.

In principle, the mirror-aiming direction would be a known function of the number of phase steps from starting positions of the electrostatic comb drives. Inasmuch as the out-of-plane bending and torsion of the flexures would generate opposing forces on beams and all the way back to the pinion gears and comb drives, there would be no gear backlash and thus no need to account for backlash in calculating or controlling the mirror-aiming direction.

This work was done by Frank T. Hartley of Caltech for **NASA's Jet Propulsion Laboratory**. *Further information is contained in a TSP [see page 1].*

NPO-30971

Linear Dynamometer With Variable Stroke and Frequency

Stroke length and frequency can be adjusted continuously during operation.

John H. Glenn Research Center, Cleveland, Ohio

An improved linear dynamometer has been developed for testing linear alternators that are to be used to convert mechanical power to electrical power in free-piston Stirling-cycle engines. Both the frequency and the length of the stroke of this dynamometer can be varied continuously, even during operation; consequently, the dynamometer can be used to fully map the capabilities of a linear alternator throughout its service envelope (its operational range as defined on a plot of limiting stroke length versus frequency) in a single test.

The dynamometer includes a balanced twin-throw eccentric crank mechanism that converts the rotary motion of a drive motor to the desired linear motion of a plunger that constitutes the moving part of the linear alternator under test. To eliminate vibration on the alternator stator, the crank mechanism also imparts an equal and opposite linear motion to a balance mass that is equal to the mass of the plunger.

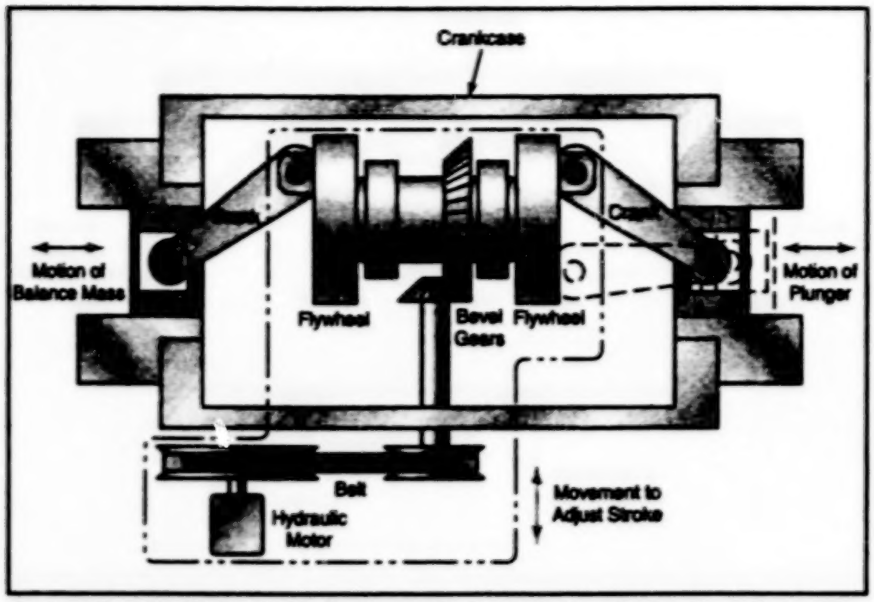

The Length of the Stroke of This Dynamometer is adjusted by adjusting the vertical position (and thus the eccentricity) of the balanced twin-throw eccentric crank mechanism.

The position of the drive-motor-and-crank assembly along a line perpendicular to the linear-stroke axis can be adjusted hydraulically to vary the eccentricity of the crank and thereby vary the length of the stroke. A compensating mechanism maintains the center of the plunger stroke with the center position of the stator. The frequency of the stroke is controlled simply by controlling the speed of the drive motor.

The dynamometer comprises four main interconnected modules: the crankcase with drive mechanism (see figure), the power pack, the operator console, and the load bank. The crankcase is an assembly of steel plates formed into a closed box enclosing the drive mechanism described above. A scavenging pump maintains a negative gauge pressure in the crankcase to minimize leakage of oil at the joints. The power pack contains a 125-horsepower (93-kW) motor that drives a compound pump that provides (1) pressurized oil for controlling the stroke and driving the hydraulic motor and (2) pressurized oil from a separate supply for lubrication.

A magnetostrictive sensor measures the displacement of the plunger. An encoder on the shaft of the hydraulic motor measures the speed. A programmable-logic controller compares the displacement and speed readings with set-point values of speed and stroke commanded via the operator console and actuates solenoid-operated servovalves to adjust the flows of oil accordingly.

The power generated by the linear alternator is dissipated in the load bank, which is a commercially available unit that presents a purely resistive load of 3 ohms and up, with selectable resistance to absorb up to 30 kW at up to 300 V. The load resistors in the load module are cooled by a fan. The load module is equipped with meters that read potential, current, frequency, and power, and with fault indicators and lockouts for fan failure, overtemperature, and overvoltage. The potential and current readings from the load bank are displayed on the operator console along with the frequency, the stroke length, the stroke-control position, and the reaction force of the stator in the alternator under test.

This work was done by George Yarr of Clever Fellows Innovation Consortium, Inc., for **Glenn Research Center.** *Further information is contained in a TSP [see page 1].*

Inquiries concerning rights for the commercial use of this invention should be addressed to NASA Glenn Research Center, Commercial Technology Office, Attn: Steve Fedor, Mail Stop 4–8, 21000 Brookpark Road, Cleveland, Ohio 44135. Refer to LEW-16951.

Books and Reports

Design Concepts for the ISS TransHab Module

Twelve reports present concepts for the design of structural and functional systems, subsystems, and components of the proposed TransHab module — an inflatable, lightweight habitation module that would be used by crewmembers of the International Space Station and would serve as a prototype of habitation modules for future spacecraft on long missions (e.g., missions to Mars). The TransHab module would be a unique hybrid structure that would combine the packaging and mass efficiencies of an inflatable structure with the advantages of a load-bearing hard structure. The governing design concept is one of a high degree of integration and multifunctionality of all parts of the TransHab system. The reports include sketches (some containing estimated dimensions) and discussions of engineering requirements. There are also numerous discussions of human factors (psychological, social, and physiological) that affect many aspects of design. Although the reports address issues specific to the TransHab module, some of the concepts discussed may be applicable to the design of temporary or transportable housing for use on Earth.

This work was done by Kriss J. Kennedy and Jasen L. Raboin of **Johnson Space Center** *and Constance M. Adams, Kurt Bush, and Jose Christian of Lockheed Martin. To obtain a copies of the reports, see TSP's [page 1].*
MSC-23090/91/181-187/189-191

Mathematics and Information Sciences

Hardware, Techniques, and Processes

47 Estimating Heterodyne-Interferometer Polarization Leakage
48 Software for Continuous Replanning During Execution
48 An Efficient Algorithm for Propagation of Temporal-Constraint Networks
49 Methodology for Tracking Hazards and Predicting Failures

Books and Reports

50 The Complexity of the Diagnosis Problem

BLANK PAGE

Estimating Heterodyne-Interferometer Polarization Leakage

Correction for the nonlinearity contributed by polarization leakage can be made in real time.

NASA's Jet Propulsion Laboratory, Pasadena, California

A method of estimating and correcting for the effect of polarization leakage on the response of a heterodyne optical interferometer has been devised. In a typical application in which a heterodyne interferometer is used as a displacement or length gauge, the effect of the polarization leakage is a nonlinearity that typically gives rise to an error of the order of 1 nm in the displacement or length. By use of the present method, it should eventually be possible, in principle, to reduce the error to the order of 10 pm or less. The technique is primarily computational and does not require any additional interferometer hardware. Moreover, the computations can be performed on almost any modern computer in real time.

The figure schematically depicts a typical heterodyne interferometer. The interferometer utilizes two laser beams with frequencies ν_1 and ν_2 that differ by a known small amount (typically, $|\nu_1 - \nu_2|$ is of the order of 1 to 100 kHz). Beams 1 and 2 are p- and s-polarized, respectively, in the reference frame of two polarizing beam splitters. Polarizers, polarization rotators, and a nonpolarizing beam splitter are used, along with the polarizing beam splitters, to separate and combine the beams at several junctions along the light path. The beams are made to interfere with each other at two photodetectors called the "reference" (R) and the "unknown" (U) photodetector, respectively. Ideally, all of the s-polarized light that arrives at the lower beam splitter makes one and only one round trip along the lower horizontal interferometer arm between two corner-cube retroreflectors, and then impinges on the U photodiode.

The difference-frequency outputs of the two photodetectors are the desired heterodyne signals. Small variations in the distance between the two retroreflectors are what one usually seeks to measure. In the ideal case, one could compute these displacements precisely from variations in the difference between the phases of the heterodyne signals from the two photodetectors. In practice, the phase measurement is degraded by noise and by systematic effects caused by imperfections in the interferometer optics. The major systematic source of error in the phase measurement is polarization leakage; that is, impingement, on the U photodetector, of (1) a small portion of the s-polarized light that passes directly through the lower polarizing beam splitter without taking the round trip between the retroreflectors and (2) another small portion of the s-polarized light that takes two or more round trips.

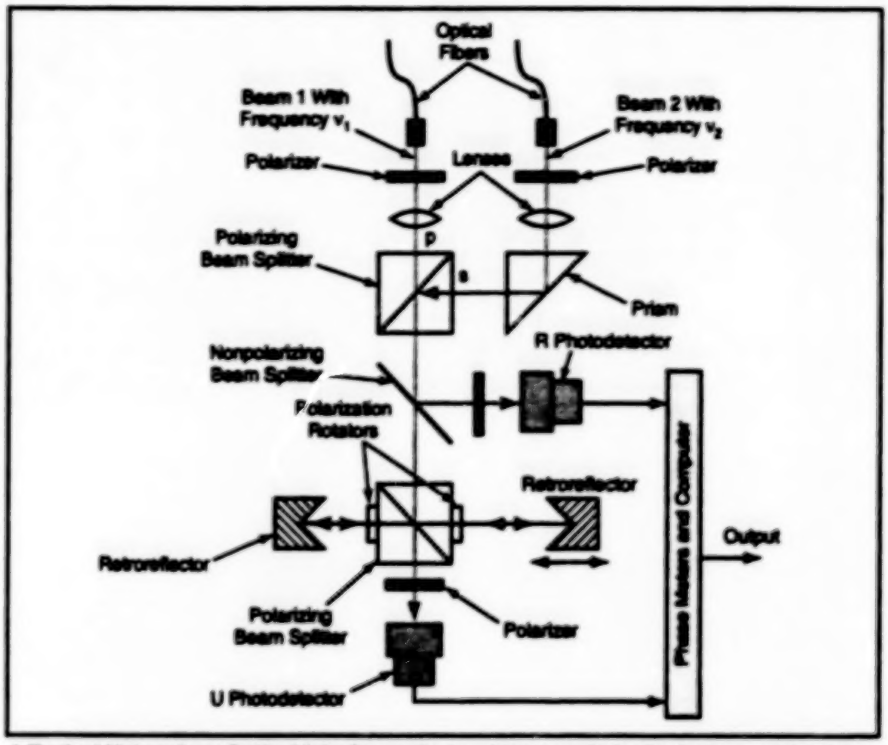

A Typical Heterodyne Optical Interferometer is subject to polarization leakage, which introduces a phase error and a corresponding nonlinearity into its response.

This polarization-leakage phase error (ε) is what gives rise to the nonlinearity in the interferometer response. The present method of estimating ε is based partly on the fact the polarization leakage is small and that ε is much less than 1 radian (as it is in cases of practical interest). A mathematical analysis shows that ε is a periodic function of ideal single-round-trip phase (ψ), and that given the aforementioned assumptions, it can be approximated by the following equation:

$$\varepsilon(\psi) = A\cos(\psi) + B\sin(\psi) + C\cos(2\psi) + D\sin(2\psi) + \ldots,$$

where A, B, C, and D are parameters to be determined in a calibration procedure summarized in the next paragraph. In order to suppress the nonlinearity to the 10-pm level, the dominant parameter in this equation must be determined to one part in 100, while the other parameters may be determined to lesser accuracy, depending on their relative amplitudes.

One of the retroreflectors is mounted on a piezoelectric transducer that can be driven by a suitable voltage to displace the retroreflector along the interferometer arm. The calibration procedure involves the use of a triangular waveform at a typical frequency of a few hertz to induce an oscillatory displacement that spans a useful number (typically ≈10) of phase cycles so that the periodic ε component of the uncorrected phase measurement becomes recognizable. The uncorrected phase measurements are sampled, filtered, and otherwise processed to extract A, B, C, and D. Then the instantaneous corrected phase measurement (which should now be a closer approximation of the desired phase ψ) is given by

$$\psi_{corrected} = \psi_{uncorrected} - \varepsilon(\psi_{uncorrected}),$$

where $\varepsilon(\psi_{uncorrected})$ is calculated by substitution of the appropriate quantities in the above equation for $\varepsilon(\psi)$.

This work was done by Alex Abramovici and Randall Bartman of Caltech for **NASA's Jet Propulsion Laboratory.** *Further information is contained in a TSP* *[see page 1].*

NPO-20906

Software for Continuous Replanning During Execution

Feedback from execution of a plan is used to update the plan continuously.

NASA's Jet Propulsion Laboratory, Pasadena, California

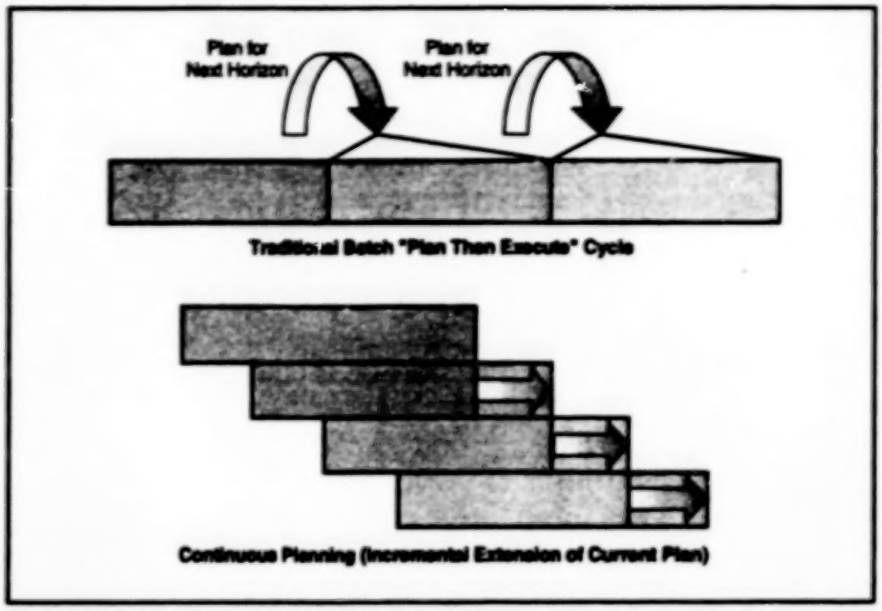
Plan for Next Horizon
Plan for Next Horizon
Traditional Batch "Plan Then Execute" Cycle
Continuous Planning (Incremental Extension of Current Plan)

Batch-Planning and Continuous-Planning Algorithms differ in their ability to respond to unforeseen circumstances. In continuous planning, the plan is updated at relatively small increments of time to keep the plan as up to date as possible.

Continuous Activity Scheduling Planning Execution and Replanning (CASPER) is a computer program for automated planning of interdependent activities within a system subject to requirements, constraints, and limitations on resources. Now at the prototype stage of development, CASPER was conceived to enable a robotic exploratory spacecraft to perform onboard, autonomous planning and replanning of scientific observations and other functions in response to diverse unanticipated phenomena that could include unknown or changing environmental conditions, equipment failures, and errors in mathematical models used in planning. On Earth, CASPER could be adapted to use in scheduling operations of production lines and other complex systems.

CASPER implements a concept of continuous planning integrated with execution, in contradistinction to the traditional concept of batch planning followed by execution. In traditional batch planning, time in the planned system is divided up into a number of relatively long planning horizons. When one nears the end of the current horizon, one projects what the state of the system will be at the end of execution of the current plan. The planning algorithm is then invoked with (1) a new set of goals for the next time horizon and (2) the projected end-of-execution state as the initial state for the next horizon. In this batch approach, planning is usually considered an off-line process that entails considerable computation, and there is significant delay from the instant when the planning algorithm is invoked to the instant when the algorithm issues a new plan. In the event of a disruption (caused, for example, by an equipment failure or an inaccurate projection of the initial state) it could be necessary to stop execution of the current plan and put the system in a safe reduced operational mode for a considerable amount of time until a new batch plan is generated. On the other hand, if a fortuitous event occurs (e.g., a planned activity is completed ahead of schedule), it may not be possible to take advantage of the opportunity thus created because it would take too long to respond with a new batch plan.

In traditional batch planning (see figure), a planning algorithm is presented with goals and an initial state. In CASPER, the planning algorithm is presented with a current set of goals, a current plan, a current state, and a model of the expected future state. At any time, the planning algorithm can be called upon to update the goals, current state, or planning horizon (at increments of time much smaller than those of batch planning) in response to an unexpected event or simply in response to the passage of time. The replanning cycle comprises the following steps:

1. Changes to the goals and the initial state are posted to the plan.
2. The effects of the changes are propagated through the current plan projections, and resulting conflicts (if any) are identified.
3. Iterative plan-repair subalgorithms are invoked to eliminate conflicts and make the plan appropriate for the current state and goals. It is these subalgorithms that make it possible to update the plan incrementally (nearly continuously) during execution in response to changing conditions and unforeseen events.

This work was done by Russell Knight, Steve Chien, Robert Sherwood, Gregg Rabideau, Darren Mutz, Tara Estlin, Forest Fisher, and Barbara Engelhardt of Caltech for **NASA's Jet Propulsion Laboratory.** *Further information is contained in a TSP [see page 1].*

This software is available for commercial licensing. Please contact Don Hart of the California Institute of Technology at (818) 393-3425. Refer to NPO-20972.

An Efficient Algorithm for Propagation of Temporal-Constraint Networks

The computational cost is much less than in prior algorithms.

NASA's Jet Propulsion Laboratory, Pasadena, California

An efficient artificial-intelligence-type algorithm for the propagation of temporal constraints has been devised for incorporation into software that performs scheduling and planning of tasks in real time. This algorithm checks for temporal consistency and computes time windows of time points within temporal-constraint networks, which are often used in scheduling and planning. A C++-language computer program that implements the algorithm has been devised for incorporation into the control software of the Mission Data System of NASA's Jet Propulsion Laboratory. The algorithm and program could also be

applied to industrial planning and scheduling problems.

For the purpose of this discussion, "time point" signifies the nominal or planned time of occurrence of a specified event in, or state of, the system (e.g., a spacecraft or a production line) that is the subject of the planning and scheduling effort. A temporal-constraint network is equivalent to a graph, the nodes of which represent time points and the lines of which represent temporal constraints. The simplest such network (see figure) contains one predecessor and one successor time point that are required to be separated by a time interval of not less than *a* and not more than *b*. In forward propagation in this network, one would endeavor to update the time window of the successor point to be consistent with the time constraint and the time window of the predecessor point; similarly, in backward propagation in this network, one would endeavor to update the time window of the predecessor point to be consistent with the time constraint and the time window of the successor point.

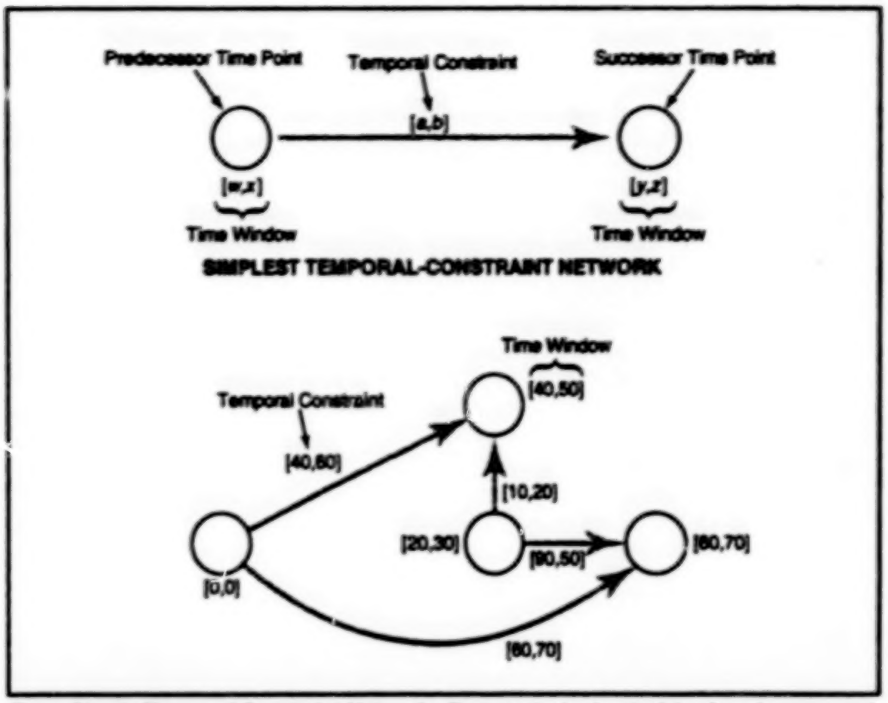

These Simple Temporal-Constraint Networks illustrate the basic principle of predecessor and successor time points joined by temporal constraints [*a*,*b*] = [minimum interval, maximum interval].

The present algorithm involves iterations of forward and backward propagation; each iteration consists of a forward sweep followed by a backward sweep. Each sweep starts the propagation of temporal constraints from a subset of time points. During the propagation, the algorithm updates the time window at each time point by use of all its incoming temporal constraints in a forward sweep or all of its outgoing temporal constraints in a backward sweep. A data structure denoted a propagation queue is used to store time points, the successors or predecessors of which are to be updated next in a forward or backward sweep, respectively. Once the time window of a time point has been updated and all its incoming (or outgoing) temporal constraints have been used, that time point is placed in the propagation queue.

A forward sweep starts from a set of time points that have no predecessors. These time points are put in the propagation queue, then the sweep proceeds until the queue is empty. The backward sweep starts from a set of time points that have no successors, and then proceeds similarly to the forward sweep. It is assumed that there are no cycles (time-constraint paths that begin and end at the same time point) so that the algorithm will not enter an infinite loop during a sweep. The algorithm performs as many iterations as are needed until either (1) there is no window left to be updated or (2) a window of negative length is created. In case (1), the final windows of all time points are considered to have been computed and the network is considered temporally consistent. In case (2), the algorithm returns the message to the effect that the network is temporally inconsistent.

The great advantage of this algorithm, relative to a prior temporal-constraint-propagation algorithm, is its computational efficiency and thus computational speed, and storage saving. The prior algorithm requires $O(N^3)$ number of arithmetic operations and $O(N^2)$ amount of memory [where $O(x)$ signifies proportionality to a quantity of the order of x and N is the number of time points in a temporal-constraint network]. In contrast, the present algorithm requires only $O(N)$ number of arithmetic operations and $O(N)$ amount of memory.

This work was done by John Z. Lou of Caltech for **NASA's Jet Propulsion Laboratory**. *Further information is contained in a TSP [see page 1].*

NPO-21098

Methodology for Tracking Hazards and Predicting Failures

This methodology can increase safety and reliability while reducing costs in all industries.

John F. Kennedy Space Center, Florida

The Continuous Hazard Tracking and Failure Prediction Methodology (CHTFPM) is a proactive methodology for gathering and analyzing information about a system in order to prevent accidents and system failures. The proactivity of the CHTFPM places it in contrast to conventional formal inductive and deductive hazard-analysis methodologies, which are limited in their effectiveness, in that they do not provide real-time information on whether the conditions in a system are becoming hazardous and could lead to a system malfunction: the conventional methodologies basically provide feedback on hazards after accidents have happened. The CHTFPM could be applied to advantage in almost all industries.

The CHTFPM involves the use of techniques from the arts of work sampling and control charting. With respect to a given system, random sampling is performed in order to detect and observe conditions, called "dendritics," that could result in accidents or unacceptable risks. The collected data are then used to generate an abstract data control chart. On the basis of the pattern of the control chart, the system is said to be "under control" (in essence, safe and thus not to be dis-

turbed) or else "out of control," in which case it is investigated for the potential emergence of hazards from the observed conditions. The results of the investigation can provide guidance for steps to be taken to ameliorate the hazardous conditions to keep the system safe.

The steps in the evaluation and correction of a system according to the CHTFPM (see figure) are the following:

1. Define the dendritics by use of the established techniques of preliminary hazard analysis (PHA), fault-tree analysis (FTA), system safety analysis (SAA), system hazard analysis (SHA), failure mode and effects analysis/critical items list (FMEA/CIL), Pareto analysis, problem reporting and corrective action (PRACA), and/or safety checklists.
2. Develop the random-sampling scheme.
3. Construct the control chart from the samples.
4. Develop a mathematical model.
5. Test the control-chart observations for actual or potential "out of control" conditions.
6. Take appropriate action to prevent or eliminate any "out of control" condition.

Step 1 is the fundamental to everything else in the CHTFPM: the effectiveness of the CHTFPM depends on the identification of the dendritics for sampling in a given system. Regarding the techniques used in step 1:

- PHA can give the analyst both the necessary introduction of the system and an initial assessment of risk, identification of safety-critical areas, and evaluation of hazards.
- The emphasis on conditions, instead of events, is the single most compelling feature of the FMEA for dendritic construction.
- The CIL, derived from the FMEA, is useful for ensuring that the most critical items are factored into dendritic construction.
- FTA can contribute to understanding of interactions among components in the system. The single most important tool for dendritic construction is the FMEA.

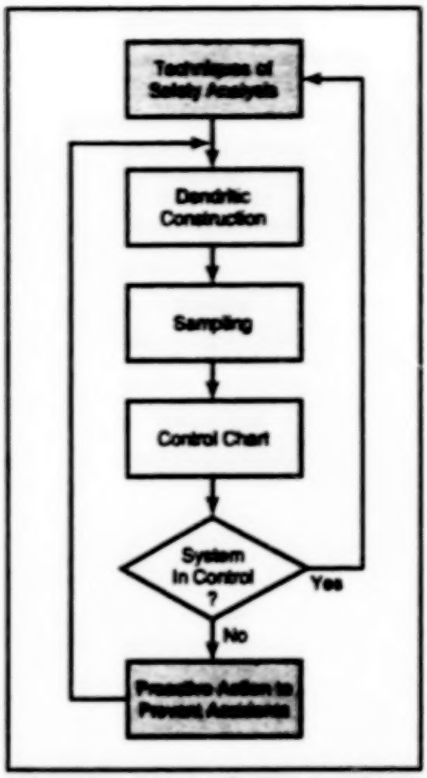

Information About a System is gathered by sampling in a prescribed manner, the information is analyzed to detect hazards, and corrective action is taken.

The sampling feature makes CHTFPM a cost-effective tool for dynamically analyzing and tracking a system for dendritics. The sampling can be performed in conjunction with other routine job functions. Sample data are used to design a control chart for use in ensuring that the system remains within an acceptable range (between the control limits); or, in other words, that it does not shift "out of control." The more representative the sample is of the process in the system, the easier it is to detect shifts.

A major problem in the CHTFPM is to choose the size and frequency of samples. In general terms, the solution must be a compromise among considerations of the cost of sampling, the loss associated with running the process out of control, and the occurrence of various system shifts attributable to natural variability (essentially, background noise) or to assignable causes (e.g., machinery malfunctions or operator errors). A process that is operating with only natural variability is said to be in statistical control. A system operating in the presence of assignable causes is said to be "out of control." The control chart provides an effective means of detecting assignable causes, identifying currently problematic areas, and predicting future problematic areas. By providing information regarding the tendency of the system, the control chart indicates when the system tends to become hazardous, facilitating the implementation of corrective steps.

This work was done by Rolando Quintana of the University of Texas for **Kennedy Space Center.** *Further information is contained in a TSP [see page 1].*
KSC-12066

Books and Reports

The Complexity of the Diagnosis Problem

A report presents a study of the complexity of an algorithm that performs model-based diagnosis of a complex hardware system. [In model-based diagnosis, an algorithm detects logical inconsistencies between observational data and a description (mathematical model) of the system.] In the study, the problem of detecting logical inconsistencies is transformed into the problem of finding prime implicants of a monotone Boolean function. This transformation enables utilization of the well-developed machinery of Boolean function theory, not directly accessible in the logical approach: one can work with monotone Boolean functions described by polynomial-size monotone circuits instead of attempting to deal with logical objects and performing exhaustive searches in order to extract all desired information. One especially notable result achieved in this study through the Boolean-function approach is the first analytical proof that the diagnosis problem is *NP*-complete. The report asserts that the discovery of the connection between diagnosis and the Boolean functions may afford new means to solve the diagnosis problem — in particular, to develop diagnostic algorithms that take super-polynomial amounts of time, in contrast to the exponential amounts of time heretofore needed to solve *NP*-complete problems.

This work was done by Farrokh Vatan of Caltech for **NASA's Jet Propulsion Laboratory.** *To obtain a copy of the report, "The Complexity of the Diagnosis Problem," see TSP's [page 1].*
NPO-30315

Life Sciences

Hardware, Techniques, and Processes

53 Externally Triggered Microcapsules Release Drugs *In Situ*

54 Combinatorial Drug Design Augmented by Information Theory

BLANK PAGE

Externally Triggered Microcapsules Release Drugs *In Situ*

Drugs can be released, at designated times, within tumors or other targets.

Lyndon B. Johnson Space Center, Houston, Texas

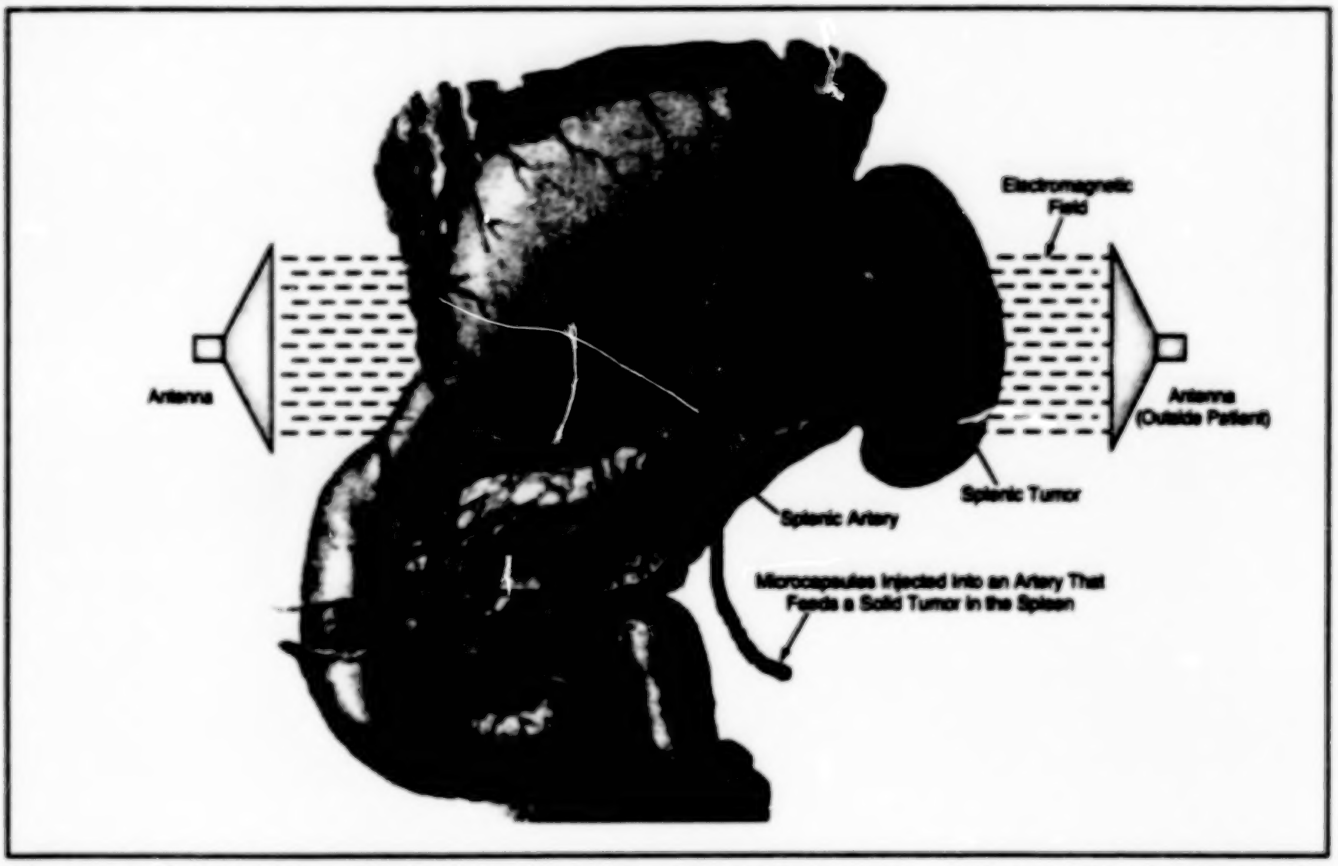

Microcapsules Containing One or More Drug(s) are injected into an artery that feeds a tumor — in this case, in the spleen. The capsules are then lysed by applying an electromagnetic field.

In an advanced method of administering drugs to target sites in human bodies, the drugs in liquid form are contained in microcapsules that are injected, and then, by exposing the target sites to externally generated electromagnetic fields, the microcapsules are lysed to release the drugs. Such externally triggered microcapsules are intended primarily for use in combined-modality therapies of cancer. In a given application, the external electromagnetic field can be applied to cause the release of the encapsulated drug(s) at a prescribed time or when the microcapsules are confirmed to be located in a specific tissue.

The concept of microencapsulation of drugs was reported in "Microencapsulation of Multiple Drugs" (MSC-22488), *NASA Tech Briefs*, Vol. 20, No. 11 (November 1996), page 92. More recently, an external-triggering method related to the present method was reported in "*In Situ* Activation of Microencapsulated Drugs (MSC-22868)," *NASA Tech Briefs*, Vol. 24, No. 9 (September 2000), page 64. A microcapsule of the type used in the present method is a multilayer structure that contains a concentrated drug solution. The outer layer of the microcapsule is a polymeric membrane that is both transparent to electromagnetic radiation and insoluble in aqueous fluids. Also contained within the microcapsule, in a compartment next to the outer membrane, is a fluid-filled compartment that contains one or more ferromagnetic thermoparticles.

The microcapsules are designed to be injected into arteries that lead to vascularized tumors or other target tissues (see figure). The outer-membrane polymer and the thermoparticle material are chosen so that the Curie temperature of the thermoparticles exceeds the melting temperature of the polymer. When the microcapsule-infused target region is exposed to an electromagnetic field of suitable frequency and power density for a specified short time (minutes), the electromagnetic field heats the thermoparticles. The localized heating of the thermoparticles melts a hole in the outer polymeric membrane, thus releasing the drug to the surrounding tissue.

Because the thermoparticles absorb the electromagnetic radiation much more strongly than do the surrounding microcapsule materials and tissues, an electromagnetic field of relatively low power can be used to effect drug release. Regulating the exposure to the electromagnetic field is not a major problem: Heating is automatically limited to the Curie temperature because above that temperature, the thermoparticles lose their ferromagnetism and thereby become less absorbent to the electromagnetic field.

The ferromagnetic material of thermoparticles can be formulated to have Curie temperatures as high as 80 °C, but because the thermoparticles are typically smaller than 1 μm, heating can be localized well enough to prevent widespread thermal damage to the surrounding tissue. Of course, depending on the application, additional therapeutic advantage might be gained by changing the frequency and/or power of the electromagnetic field, after the microcapsules have been lysed, to obtain controlled hyperthermia to enhance the local effective-

ness of the drugs that have been released. In some applications, it could be desirable to effect multiple releases of the same drug or different drugs by use of injecting mixtures of microcapsules containing ferromagnetic particles with different Curie temperatures that could be triggered at different times, as determined by the strength of the electromagnetic field and the duration of exposure.

This work was done by Dennis R. Morrison and Benjamin Mosier of **Johnson Space Center.** *Further information is contained in a TSP [see page 1].*

This invention is owned by NASA, and a patent application has been filed. Inquiries concerning nonexclusive or exclusive license for its commercial development should be addressed to the Patent Counsel, Johnson Space Center, (281) 483-0837. Refer to MSC-22939.

Combinatorial Drug Design Augmented by Information Theory

It may be possible to suppress drug-resistant viruses.

NASA's Jet Propulsion Laboratory, Pasadena, California

A proposed method of designing antiviral drugs provides for the utilization of combinatorial-chemistry techniques that have been used previously for this purpose, in conjunction with applicable principles of information theory. In its information-theoretic aspect, the method can be characterized as one of maximizing the mutual information between (1) ensembles of drugs and (2) ensembles of viruses that one seeks to combat by use of the drugs (denoted in the art as targets). The method would entail increases in the time and cost of development of drugs, but these disadvantages could be offset by reduction or prevention of the emergence of drug-resistant viral populations.

Heretofore, it has been standard practice to design an antiviral drug to bind to a "consensus-sequence" protein of a viral species or target ensemble. However, consensus-sequence proteins are conceptual only; they do not occur in nature. In treatment-naive patients (that is, patients who have not taken the drug), many viral targets are polymorphic, such that the drug is not specific to many of the mutants in the target population. As a consequence, the drug-resistant mutants quickly become the dominant species in the viral population; in other words, the viral targets become drug-resistant.

The proposed method is based partly on recognition that the ensemble of proteins of a viral target forms a "quasispecies" of mutants characterized by a particular entropic profile. Hence, one should have a greater chance of suppressing the rise of drug-resistant mutants through combinatorial design of a drug to combat the quasispecies, rather than the consensus-sequence species. One would seek a drug that binds not only to the consensus target but also to its mutants. Depending on the viral target, the most effective drug might, itself, be a quasispecies in that it would be an ensemble of drugs.

An ensemble of drugs with substitution probabilities complementary to those of the entropic profile of the target could be even more effective. Such an ensemble of drugs could be designed in a procedure that minimizes the conditional target entropy. In such a procedure, combinatorial ensembles of drugs would be used on mixtures of targets prepared according to the treatment-naive substitution probabilities. In a sequence of "passes," the target ensemble would be treated with a drug ensemble and then resequenced to measure the remaining entropy of the target ensemble, given the drug ensemble. By use of a suitable algorithm, the combinatorial drug ensemble could then be modified in further steps until the conditional target entropy was minimal, at which point the drug ensemble could be considered optimal.

This work was done by Christoph Adami of Caltech for **NASA's Jet Propulsion Laboratory.** *Further information is contained in a TSP [see page 1].*

In accordance with Public Law 96-517, the contractor has elected to retain title to this invention. Inquiries concerning rights for its commercial use should be addressed to

Intellectual Assets Office
JPL
Mail Stop 202-233
4800 Oak Grove Drive
Pasadena, CA 91109
(818) 354-2240
E-mail: ipgroup@jpl.nasa.gov

Refer to NPO-30252, volume and number of this NASA Tech Briefs *issue, and the page number.*

END

09-10-02